# Lymphatic Invasion of Plakoglobin-Dependent Tumor Cell Clusters Drives Formation of Polyclonal Lung Metastases in Colon Cancer

Emre Küçükköse,[1] Jamila Laoukili,[1] Alexander N. Gorelick,[2] Sebastian Degner,[2] Miangela M. Laclé,[3] Lotte van den Bent,[1] Niek A. Peters,[1] André Verheem,[1] Wei-Ting Hung,[2] Nicola C. Frenkel,[1] Emma C. E. Wassenaar,[1] Nico Lansu,[4,5] Kristiaan J. Lenos,[4,5,6] Louis Vermeulen,[4,5,6] Miriam Koopman,[7] Jeanine M. L. Roodhart,[1,7] Geert J. P. L. Kops,[4,5] Inne H. M. Borel Rinkes,[1] Jeroen Hagendoorn,[1] Kamila Naxerova,[2] and Onno Kranenburg[1,8]

[1]Division of Imaging and Cancer, Laboratory of Translational Oncology, University Medical Center Utrecht, Utrecht, The Netherlands; [2]Center for Systems Biology, Massachusetts General Hospital and Harvard Medical School, Boston, Massachusetts; [3]Department of Pathology, University Medical Center Utrecht, Utrecht, The Netherlands; [4]Oncode Institute, Royal Netherlands Academy of Arts and Sciences, Utrecht, The Netherlands; [5]Hubrecht Institute, University Medical Center Utrecht, Utrecht, The Netherlands; [6]Center for Experimental and Molecular Medicine, Amsterdam University Medical Center, Amsterdam, The Netherlands; [7]Division of Imaging and Cancer, Department of Medical Oncology, University Medical Center Utrecht, Utrecht, The Netherlands; and [8]Utrecht Platform for Organoid Technology, Utrecht University, Utrecht, The Netherlands

Colon   Liver   Lungs

Plakoglobin   Lymphatic vessel   Blood vessel

Gastroenterology
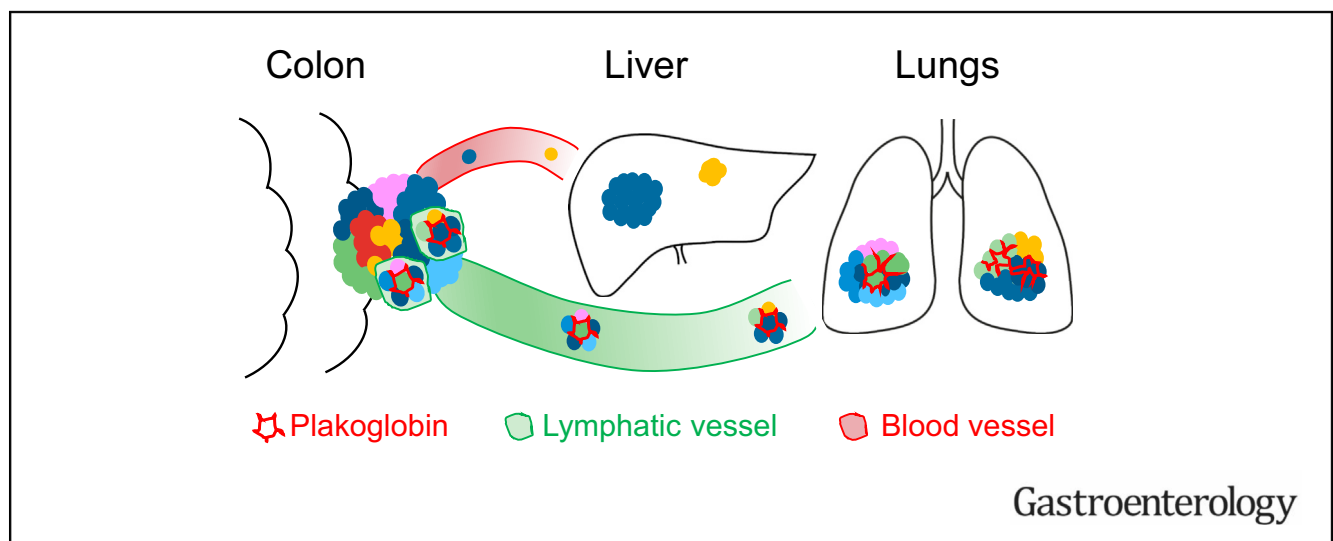
BACKGROUND & AIMS: Patients with colon cancer with liver metastases may be cured with surgery, but the presence of additional lung metastases often precludes curative treatment. Little is known about the processes driving lung metastasis. This study aimed to elucidate the mechanisms governing lung vs liver metastasis formation. **METHODS:** Patient-derived organoid (PDO) cultures were established from colon tumors with distinct patterns of metastasis. Mouse models recapitulating metastatic organotropism were created by implanting PDOs into the cecum wall. Optical barcoding was applied to trace the origin and clonal composition of liver and lung metastases. RNA sequencing and immunohistochemistry were used to identify candidate determinants of metastatic organotropism. Genetic, pharmacologic, in vitro, and in vivo modeling strategies identified essential steps in lung metastasis formation. Validation was performed by analyzing patient-derived tissues. **RESULTS:** Cecum transplantation of 3 distinct PDOs yielded models with distinct metastatic organotropism: liver only, lung only, and liver and lung. Liver metastases were seeded by single cells derived from select clones. Lung metastases were seeded by polyclonal clusters of tumor cells entering the lymphatic vasculature with very limited clonal selection. Lung-specific metastasis was associated with high expression of desmosome markers, including plakoglobin. Plakoglobin deletion abrogated tumor cell cluster formation, lymphatic invasion, and lung metastasis formation. Pharmacologic inhibition of lymphangiogenesis attenuated lung metastasis formation. Primary human colon, rectum, esophagus, and stomach tumors with lung metastases had a higher N-stage and more plakoglobin-expressing intra-lymphatic tumor cell clusters than those without lung metastases. **CONCLUSIONS:** Lung and liver metastasis formation are fundamentally distinct processes with different evolutionary bottlenecks, seeding

entities, and anatomic routing. Polyclonal lung metastases originate from plakoglobin-dependent tumor cell clusters entering the lymphatic vasculature at the primary tumor site.

GI CANCER

C olon cancer is the second most common cause of cancer-related mortality worldwide. Mortality is largely due to the formation of distant metastases, which occur most frequently in the liver, lungs, and peritoneal cavity.[1] In patients with metastases confined to the liver, extensive local and systemic treatment can achieve 5-year survival rates of >50%.[2] However, the presence of additional extrahepatic metastases, mostly in the lungs, often precludes local treatment and may result in unrelenting disease progression.[3–5] A thorough understanding of the principles of lung metastasis formation in colon cancer is needed to optimize treatment strategies.

In the classical model of colon cancer metastasis, disseminated tumor cells enter the portal system via the mesenteric veins, after which they get trapped in the hepatic microvasculature to form liver metastases.[6] Indeed, in patients with metastatic colon cancer, circulating tumor cells are detected at much higher frequency in the portal vein compared with the systemic circulation.[7,8] Tumor cells disseminating from liver metastases can be detected with high frequency in hepatic venous blood,[7,9] after which they could theoretically seed secondary lung metastases in a sequential fashion.[6,7] However, paired genetic analysis of liver and lung metastases in individual patients with colon cancer revealed that most lung metastases originated from a different subclone within the primary tumor than the liver metastases.[10] Moreover, lung metastases frequently occur in the absence of liver metastases.[3,11,12] These findings cannot be explained by a sequential liver-to-lung metastasis model, and imply that additional mechanisms of lung metastasis formation must exist.

The lymphatics provide an alternative route for tumor cell dissemination. In mouse models for various cancer types, lung metastases were initiated by tumor cells disseminating from local lymph node metastases.[13,14] Whether lymphatic dissemination plays a role in the formation of lung metastases in colon cancer is unknown. Pairwise genetic analysis of clinical samples from patients with colon cancer revealed a common subclonal origin of lymph node and distant metastases (liver and omentum) in 35% of the cases.[15] This suggests that, also in colon cancer, onward spread from local lymph node metastases may seed distant metastases. Pairwise genetic analysis of clinical tumor samples provides insight into the evolutionary relationships among primary and metastatic tumor lesions in individual patients, but does not measure cell biological processes, such as invasion and intra- and extravasation, and cannot be used for functional studies on metastasis competence. Mouse models in which lung metastases develop spontaneously from orthotopically implanted tumor cells have been described previously,[16,17] but a detailed

WHAT YOU NEED TO KNOW

BACKGROUND AND CONTEXT

The presence of lung metastases often precludes curative treatment in patients with metastatic gastrointestinal cancer. Insight into the pathways governing lung metastasis formation may help to rationally improve treatment strategies.

NEW FINDINGS

Fundamentally distinct processes drive lung and liver metastasis formation, with different evolutionary bottlenecks, seeding entities, routing, and clonal composition. Lung metastases originate from plakoglobin-dependent tumor clusters entering the lymphatic vasculature.

LIMITATIONS

Metastatic colon cancer was initiated by implantation of human tumor-derived organoids into the cecum of immune-deficient mice. We were, therefore, unable to investigate the role of immune cells in organ-specific metastasis.

CLINICAL RESEARCH RELEVANCE

Distinct mechanisms underlie liver and lung metastasis formation, yielding genetically distinct metastases. This highlights the need for developing organ site–specific metastasis prediction, prevention, and treatment strategies. The formation of plakoglobin-expressing tumor clusters in primary gastrointestinal cancers defines a subgroup of tumors with high propensity to form lung metastases. This group may benefit from extensive lymph node dissection and/or adjuvant therapy.

BASIC RESEARCH RELEVANCE

Lung metastases in colon cancer are initiated by lymphatic invasion of plakoglobin-dependent tumor cell clusters, frequently containing genetically distinct subclones. Within such clusters, metastatic competence becomes a shared trait. The results identify a role for plakoglobin and hence desmosomes, in determining intra- and inter-metastatic heterogeneity in an organ-site–dependent manner. Desmosomes characterize lung but not liver metastases, potentially generating phenotypic diversity.

understanding of the mechanisms governing lung metastasis formation in colon cancer is currently lacking.

Here, we applied microsurgical implantation of patient-derived organoids (PDOs)[18–20] into mice to generate colon tumors metastasizing spontaneously to the lungs, liver, or

Most current article

both organs. Lung metastases were seeded by means of polyclonal plakoglobin-dependent tumor cell clusters entering the lymphatic vasculature and disseminating through the mesenteric lymphatic system, bypassing the liver. Targeting VEGFR3 reduced the number of lymphatic tumor vessels and suppressed lung metastasis formation. The results delineate a specific therapeutically targetable pathway governing lung metastasis formation in colon cancer.

Materials and Methods

Human Tissues

All experiments with human tissues were approved by the Biobank Research Ethics Committee (protocol numbers 12–093 and 18-566) of the University Medical Center Utrecht (Utrecht, The Netherlands). Written informed consent from the donors for research use of tissue in this study was obtained before acquisition of the specimen.

In Vitro Organoid Culture

Tumor PDO1 was obtained from Hubrecht Organoid Foundation (original nomenclature is HUB-02-C2-098). PDO2 and PDO3 were established previously.[21] Culturing PDOs was performed by embedding into ice-cold Matrigel (Corning), mixed with a colorectal cancer (CRC) culture medium (Supplementary Table 1) in a 3:1 ratio. For passaging, the tumor organoids were dissociated with TrypLE Express (Gibco, Breda, The Netherlands, no. 12604021) for 5–10 minutes at 37°C and replated in a prewarmed 6-well plate. Rho-associated kinase inhibitor Y-27632 (Tocris, Abingdon, UK, no. 1254, 10 μM) was added to culture medium upon plating for 2 days.

Optical Barcoding

The PDOs were simultaneously transduced with 3 red-green-blue constructs (each encoding for a color) according to a previously published protocol.[22] The following lentiviral gene ontology (LeGO) vectors were used: LeGO-C2 (27339), LeGO-V2 (27340), and LeGO-Cer2 (27338) (Addgene). Briefly, lentiviral production was performed by calcium phosphate transfection protocol in human embryonic kidney 293T cells using the transfer plasmid (15 μg), pMD2.G (12259, 7.5 μg), and psPAX2 (12260, 7.5 μg). The following day, medium was replaced by advanced Dulbecco's modified Eagle medium/F12 medium (Invitrogen) supplemented with HEPES buffer (Lonza, 10 mM), penicillin/streptomycin (Gibco, 50 U/mL), and Gluta-MAX (Gibco, 2 mM). The next day, 50,000 single cells of PDOs were resuspended in the virus medium (which was filtered through 0.45-μm polyethersulfone filter), supplemented with Polybrene (Sigma-Aldrich, 8 μg/mL), N-acetylcysteine (Sigma-Aldrich, 1.25 mM), and Rho-associated kinase inhibitor Y-27632 (Sigma-Aldrich, 10 μM), and incubated overnight at 37°C, 5% (vol/vol) CO_2 on nonadherent plates (ultra-low attachment surface; Sigma-Aldrich). After 24-hour incubation, cells were washed twice in phosphate-buffered saline (Sigma-Aldrich) and cultured as described above. The PDOs were sorted based on YeGr2-A (mCherry), blue 1-A (Venus), and Violet1-A (Cerulean) expression at least 2 passages after transduction on a fluorescence-activated cell sorting Aria II (BD Biosciences) machine (Supplementary Table 2).

Animal Experiments

The project proposals (614-01-07 and 15055-1-10) for studies involving laboratory animals were approved by Utrecht University's Animal Welfare Body and Animal Ethics Committee and licensed by the Central Authority for Scientific Procedures on Animals (license AVD115002016614). All experiments were conducted in accordance with the Dutch Experiments on Animals Act, in line with European Directive 2010/63/EU and by licensed personnel.

In order to evaluate the spontaneous metastatic capacity of the tumor PDOs, we used the murine orthotopic cecum implantation model.[23] In summary, the day before implantation, PDOs were dissociated into single cells and 2.5×10^5 cells were plated in 10-μL drops of neutralized Collagen I High Concentration Rat Tail (Corning). PDOs were allowed to recover overnight at 37°C, 5% (vol/vol) CO_2. NOD.Cg-Prkdc^{SCID} Il2rg^{tm1Wjl}/SzJ (NSG) male mice between 8 and 10 weeks of age were treated with a subcutaneous dose of carprofen (5 mg/kg, Rimadyl, Utrecht University Veterinary Pharmacy) 30 minutes before surgery and were subsequently sedated using isoflurane inhalation anesthesia (approximately 2% [vol/vol] isoflurane/O_2 mixture). The cecum was exteriorized through a midline abdominal incision and a single collagen drop containing the PDOs was microsurgically transplanted into the cecal submucosa. Carprofen was given 24 hours post surgery. Targeting of the lymphatic vasculature in vivo was performed by injecting mF4-31C1[24] (anti-mVEGFR3: 625 μg, 100 μL; kind gift from Eli Lilly) intraperitoneal 3 times per week, starting 3 days post surgery. The humane end point for all animals was reached after 4–6 weeks. Organs were harvested for further analysis.

Results

Spontaneous Colon Cancer Metastasis Models With Distinct Organotropism

To generate models for spontaneous metastasis formation to the liver and lungs, we selected PDOs from patients with colon cancer with liver metastases (PDO1) or lymph node and lung metastases (PDO2). In addition, we selected a PDO from an anonymous donor that, after transplantation, gave rise to both liver and lung metastases (PDO3). All 3 PDOs were embedded in collagen drops and were transplanted orthotopically into the submucosa of the cecum of NSG mice[23] (Supplementary Figure 1*A* and *B*). All PDOs formed primary tumors at the implantation site (Supplementary Figure 1*C*). In all models, distant metastases developed 4–6 weeks after implantation, but with different patterns of spread; PDO1 tumors metastasized to the liver, PDO2 tumors metastasized to the lungs, and PDO3 tumors metastasized to both liver and lungs (Supplementary Figure 1*D* and *E*). NSG mice do not develop lymph nodes, precluding the analysis of lymph node metastases.

Optical Barcoding Reveals Intra-Lesion Heterogeneity in Lung Metastases, but Not Liver Metastases

Optical barcoding using multicolor (red-green-blue) LeGO vectors[22] allows the tracing of individual cells and

their progeny in in vivo models. We applied this technology to study clonal processes during primary tumor growth and metastasis formation (Figure 1A and B). Transduction of PDO1–3 with the 3 LeGO vectors yielded PDO cultures in which individual cells were labeled with a wide range of unique colors. The specific color in each cell is stochastically determined by the number of vector copies inserted and by the genomic site of insertion[22] (Figure 1C). After excluding unlabeled cells using fluorescence-activated cell sorting

(Supplementary Figure 2), the PDO-LeGO cultures were transplanted into the cecum of NSG mice.

Confocal microscopy analysis of the primary tumors in all 3 models showed a high color diversity, with a clear demarcation of individually growing (monochromatic) clones, but also regions with a mixed (polychromatic) growth pattern (Figure 1D). Most (95%) liver metastases in models PDO1 and PDO3 consisted of a single color, indicating seeding by a single cell. Only 5% of liver metastases
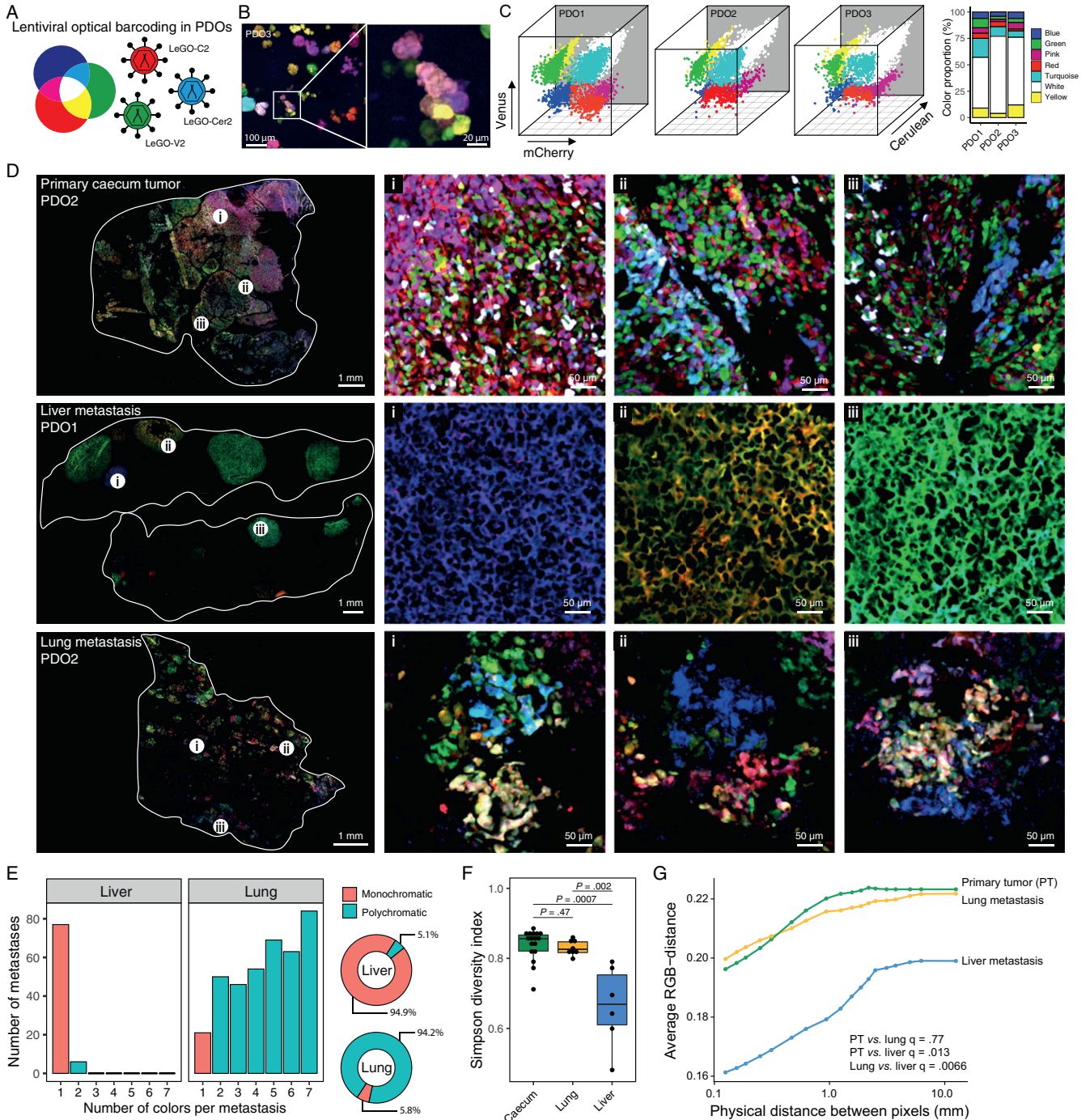
consisted of 2 colors. No liver metastases were found consisting of more than 2 colors. By contrast, most (94%) lung metastases in models PDO2 and PDO3 consisted of 2–7 different colors, and only 6% were monochromatic (Figure 1D and E). In the PDO3 model, monochromatic liver metastases and polychromatic lung metastases developed simultaneously within the same mouse (Supplementary Figure 3).

Clone Selection During Liver Metastasis Formation but Not Lung Metastasis Formation

Optical barcoding can also be used to calculate the fraction of "transferred color diversity" from the primary tumor to the (entire) liver and lung. This measure provides information on the fraction of metastasis-competent clones growing within the primary tumor. We found that the fraction of colors transferred from the primary tumor to the liver is significantly lower than the fraction of colors transferred to the lungs (Figure 1F). Indeed, most color-coded clones that were present in the primary tumors contributed to the formation of lung metastases, indicating a low selection pressure. By contrast, liver metastases were formed by single cells from a significantly lower number of individual color-coded clones, indicating higher selection pressure. Moreover, analysis of color distributions using whole-organ red-green-blue images revealed that pixels of distinct colors were in closer proximity in primary tumors and lung metastases than in liver metastases (Figure 1G). These analyses confirm both the polychromatic nature of individual lung metastases and the higher transfer of color diversity during lung vs liver metastasis formation in the entire organ (Figure 1G).

Lung Metastasis Competence Is Associated With Invasion of Lymphatic Vessels by Multicolored Tumor Cell Clusters

Recently, we demonstrated that lymph node metastases display significantly higher inter-lesion and intra-lesion heterogeneity than liver metastases.[25] The similarities between lung and lymph node metastases (ie, a wide evolutionary bottleneck and high intra-lesion heterogeneity) prompted us to study whether lung metastases could result from lymphatic dissemination. First, we investigated the presence of blood and lymphatic vessels in the primary tumors derived from PDO1-3. Immunohistochemistry (IHC) using anti-CD31 (blood endothelial cells) and anti-LYVE1 (lymphatic endothelial cells) revealed that primary PDO1 tumors displayed a significantly higher blood vessel density than PDO2 and PDO3 tumors and PDO2 and PDO3 tumors displayed a significantly higher intra-tumor lymphatic vessel density. In both PDO2 and PDO3 primary tumors, the lymphatic vessels contained clusters of tumor cells. By contrast, lymphatic vessels in PDO1 tumors were located outside the tumor mass and lacked tumor cells (Figure 2A and B).

Confocal microscopy analysis revealed that lymphatic vessels were infiltrated by polychromatic tumor cell clusters (Figure 2C). The median color Simpson Diversity Index of all cell clusters residing within the lymphatic vessels was similar to the color Simpson Diversity Index of the corresponding primary tumors (0.81 and 0.77, respectively) (Figure 2D). These data indicate that lymphatic invasion does not pose a significant barrier to most tumor cells in the primary tumor, consistent with what is observed in clinical lymph node metastasis samples.[25]

To identify differences between the 3 PDO models that might further explain their distinct metastatic organotropism, we performed RNA sequencing of the primary tumors. Previous work had identified a signature that distinguishes circulating tumor cell clusters from circulating single tumor cells. This signature is pre-existent within primary tumors and predicts tumor cell cluster–mediated dissemination and metastasis.[26] We found that the tumor cell cluster signature score was significantly higher in primary tumors giving rise to lung metastases (PDO2 and PDO3) than in primary tumors giving rise to liver metastases (PDO1) (Figure 2E and F). Lymphatic drainage of colon tumors occurs through the mesenteric lymphatic system. To search for tumor cells or clusters within the tumor-draining lymphatics, we fixed and embedded the entire mouse colon,

---

Figure 1. Lung metastases are characterized by high intra-lesion heterogeneity and the absence of clone selection. (*A*) Schematic overview of the optical barcoding system including 3 lentiviral vectors. Each vector encodes for a different fluorescent protein: LeGO-C2 (mCherry;red), LeGO-V2 (Venus;green), and LeGO-Cer2 (Cerulean;blue). Mixing of the 3 basic colors red, blue, and green leads to the generation of the whole color spectrum, which facilitates clonal tracking by marking each cell with a different color. (*B*) Representative *image* of PDO3 transduced with LeGO vectors. (*C*) *Scatter 3-dimensional plots* are depicting on each axis the intensity of mCherry (*X*), Venus (*Y*), and Cerulean (*Z*) of fluorescence-activated cell sorting analysis from the LeGO-transduced PDOs. *Stacked bar plots* demonstrate identified color populations based on binning the color spectrum generated in the PDOs. (*D*) Representative whole-tissue confocal images of LeGO primary tumor, liver, and lung metastases in the orthotopic implantation models. (*E*) *Bar graphs* represent the number of metastases containing 1 (*red bars*) or multiple (*blue bars*) colors detected in the liver or lungs. *Pie charts* represent the proportion of total metastatic burden associated with monochromatic (*red*) or polychromatic (*blue*) metastases. (*F*) *Box plots* represents the Simpson Diversity Index (SDI) scores, a measure for diversity of colors in each primary cecum tumor, liver, and lung image. The SDI takes into account the number of species (ie, unique colors) present, as well as the relative abundance of each species. A higher SDI represents a more diverse population. Mann-Whitney U test with Bonferroni correction was applied. (*G*) Distance-based measure of color diversity in whole tissues. Physical Euclidean distances between *xy* coordinates of randomly sampled pixels are calculated together with the respective distances in red-green-blue (RGB) space relative to the maximum obtainable Euclidean distance in RGB. For all pixel pairs that are at most a given distance apart (x-axis), the median relative distance in RGB is calculated, followed by averaging over all images from the same mice and lesion type. The average over all mice is calculated and presented. Holm–Bonferroni method was applied.
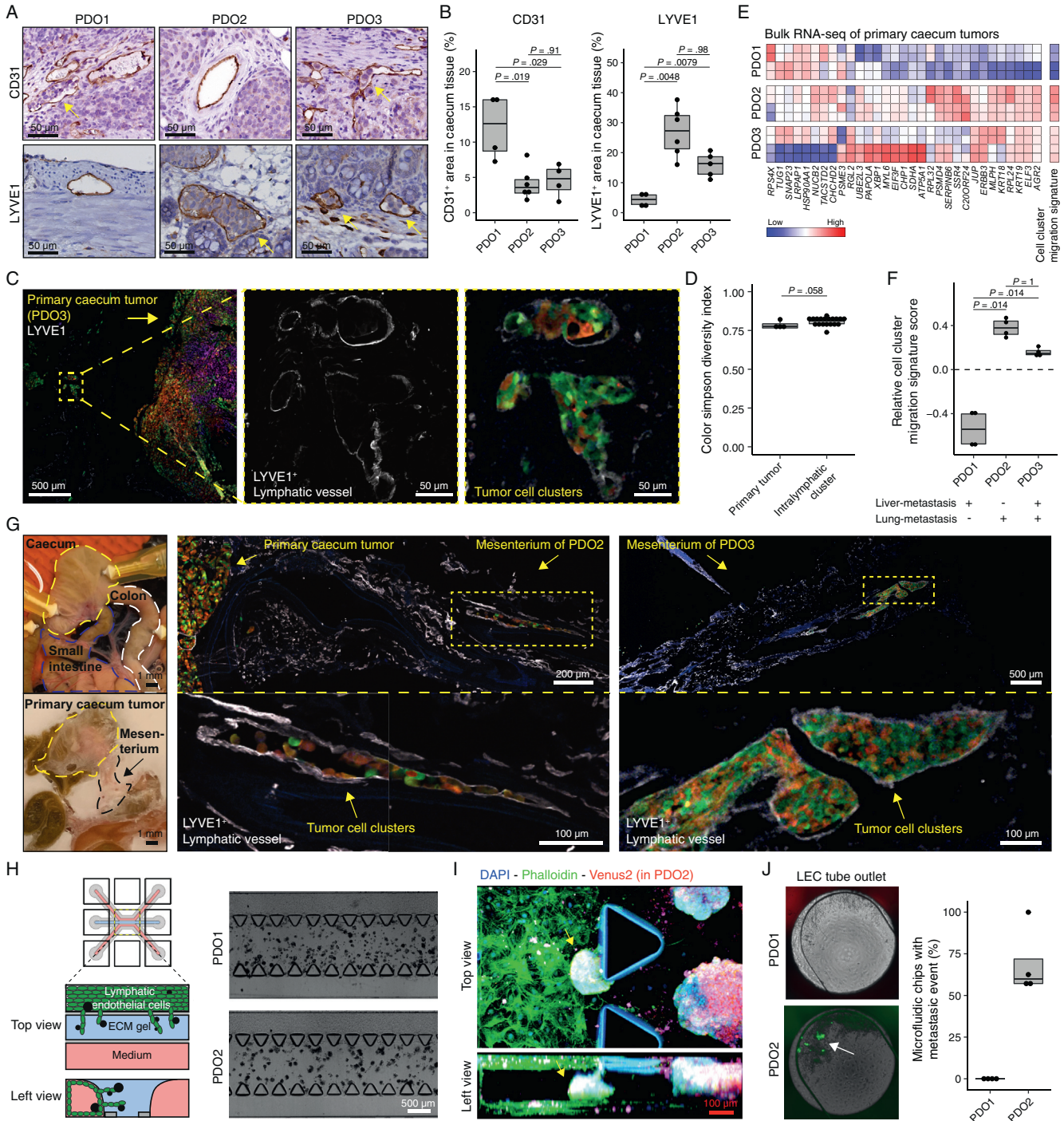
Figure 2. Lung metastasis competence is associated with lymphatic invasion by polyclonal tumor cell clusters. (*A*) Representative CD31 (*top*) and LYVE1 (*bottom*) IHC staining of primary cecum tumors for the 3 different PDO orthotopic implantation models. *Yellow arrows* indicate tumor cells in vessels. (*B*) Relative quantification of CD31 and LYVE1 area (%) in total tissue. n = 4 NSG mice per model. Mann-Whitney U test was applied. (*C*) Representative *image* (*left*) of LeGO-PDO2–initiated primary cecum tumor with LYVE1 staining (*middle*) and (*right*) overlay *image* showing multicolored tumor cell clusters within a lymphatic LYVE1+ vessel. (*D*) *Box plots* represents the SDI of the detected intra-lymphatic tumor cell clusters and their corresponding primary cecum tumors. (*E*) *Heatmap* showing the expression of a gene signature for "tumor cell cluster migration"[26] in whole-exome (RNA) sequencing data of primary cecum tumors and (*F*) *box plot* represents the relative score. (*G*) En-bloc fixation on the complete mouse digestive system and LYVE1 immunofluorescence staining with multicolored tumor cell clusters in lymphatic vessels. (*H*) Schematics of 3-lane OrganoPlate configuration: top perfusion channel (medium), middle extracellular matrix channel (Matrigel), and bottom perfusion channel (medium containing lymphangiogenic mix). Lymphatic endothelial cells (LECs) form a monolayer tube in the top perfusion channel. PDOs are cultured in the middle channel. (*I*) immunofluorescence staining with 4′,6-diamidino-2-phenylindole (DAPI), phalloidin, and endogenous expression of Venus2 in PDO2. *Top* and *left view* of a 3-dimensional *image* of PDOs (*yellow arrows*) invading the LEC tube. (*J*) LEC tube outlet, representative for degree of invasion and metastatic event, shown at day 10 of experiment. *Box plot* show the frequency of metastatic events observed in the outlets. Mann-Whitney U test was applied.
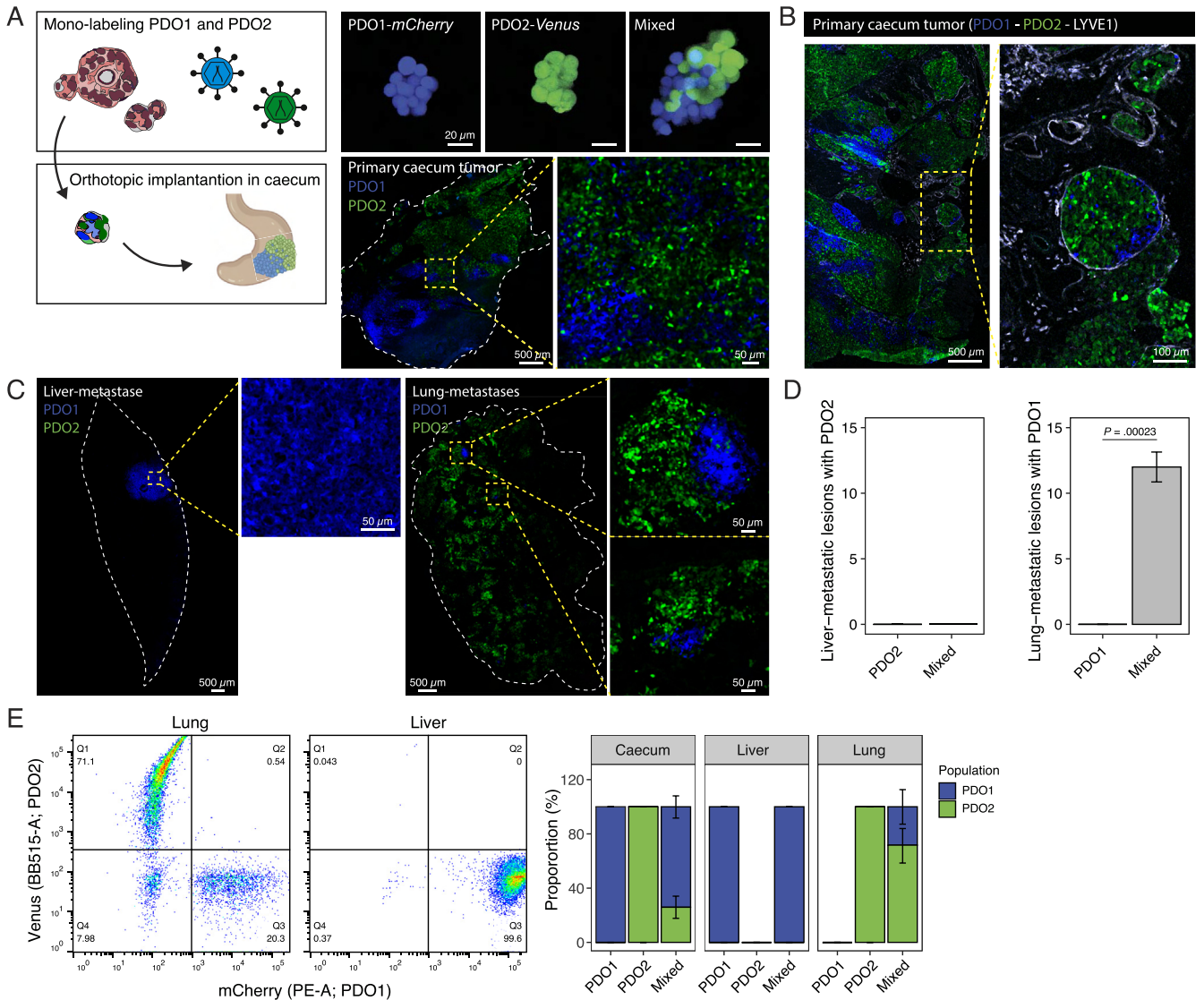
Figure 3. Transfer of lung metastasis competence within polyclonal tumor cell clusters. (*A*) Experimental setup: PDO1 (liver metastases–competent only) are labeled with LeGO-C2 and PDO2 (lung metastases–competent only) with LeGO-V2. Mono-labeled PDOs are mixed (1:1 ratio) in vitro and orthotopically implanted in the cecum of NSG mice. *Top confocal images* represent in vitro hybrid organoid consisting of PDO1 (*blue*) and PDO2 (*green*) cells. For visualization, *blue* instead of *red color* has been shown. *Bottom confocal images* represent the composition of a hybrid-organoid–initiated primary cecum tumor. (*B*) Representative confocal *image* showing tumor cell cluster with PDO1 and PDO2 cells intravascular in a lymphatic vessel (LYVE1^{+}). (*C*) Representative confocal *images* for (*left*) liver and (*right*) lung metastases originated from hybrid-organoid primary tumor. (*D*) Liver and lung metastases composition quantification, measured by scoring presence of the 2 distinct PDOs in metastases based on color. N = 5 mice. Mann-Whitney U test was applied. (*E*) Flow cytometry analysis of PDO presence in liver and lung metastases. PDO1-mCherry and PDO2-V2 are detected by PE-A and BB515-A, respectively. *Stacked bar plots* represent proportional composition of both PDOs in primary cecum tumor, liver, and lung tissue (N = 5 mice).

containing PDO-initiated primary cecum tumors and the surrounding mesentery (Figure 2*G*). Immunofluorescence analysis of LYVE1 expression combined with fluorescence analysis of LeGO-labeled tumor cells revealed the presence of polychromatic tumor cell clusters within lymphatic vessels, clearly separated from the primary tumor in models PDO2 and PDO3, but not in PDO1 (Figure 2*G* and Supplementary Figure 4). Thus, polychromatic tumor cell clusters leave the primary tumor through the mesenteric lymphatic vasculature.

The presence of tumor cell clusters within LYVE1^{+} vessels in the PDO2 and PDO3, but not PDO1, tumors

indicated that there may be a tumor cell–intrinsic difference between their capacities to invade lymphatic vessels. To test this, we used PDO1 and PDO2 in a microfluidic system[27] in which tumor organoids grow juxtaposed to a perfused 3-dimensional tube of immortalized lymphatic endothelial cells (Figure 2*H*). Clusters of PDO2 cells readily invaded the lymphatic endothelial cells tube, giving rise to "in vitro metastasis" events, and PDO1 cells did not (Figure 2*I* and *J*). Thus, a high density of intra-tumor lymphatic vessels and the ability of tumor cell clusters to invade such vessels determine lung metastasis competence in the PDO models.

Transfer of Lung Metastasis Competence Between Genetically Distinct Tumor Cells Residing Within Clusters

Tumor cell clusters invading lymphatic vessels may consist of more than 1 genetic subclone, which may result in the generation of polyclonal lung metastases. To study this, we generated PDO1 (mCherry), PDO2 (Venus), and hybrid PDO1/PDO2 primary tumors. Fluorescence analysis of sections of the generated hybrid tumors showed that both PDOs were present as single-clone/color expansions, but regions of intermixed growth also existed (Figure 3A). Immunofluorescence analysis of primary tumor sections further showed that tumor cell clusters containing both colors/clones were present within LYVE1^{+} lymphatic vessels (Figure 3B). Fluorescence analysis of lung metastases showed that PDO1 cells were never observed in the lungs of mice with primary PDO1 tumors. However, in mice with primary hybrid PDO1/PDO2 tumors, 12% of the lesions now consisted of both PDO1 and PDO2 cells. Thus, PDO2 cells facilitated lung metastasis formation by PDO1 cells, which were not capable of that on their own (Figure 3C and D). By contrast, all liver metastases in mice with either PDO1 or PDO1/PDO2 hybrid tumors consisted of PDO1 cells exclusively. To quantify the carry-over phenomenon further, we performed fluorescence-activated cell sorting analysis of PDO1 and PDO2 cells in paired lung and liver tissues of mice with PDO1, PDO2, or PDO1/PDO2 hybrid tumors. This revealed that PDO1 cells were absent in the lungs of mice with PDO1 tumors, but contributed extensively (20%) to lung metastasis formation in mice with hybrid PDO1/PDO2 tumors (Figure 3E). All liver metastases in mice with either PDO1 or PDO1/PDO2 hybrid tumors consisted of PDO1 cells exclusively. Thus, lung metastasis competence can be transferred among groups of genetically distinct tumor cells through the formation of tumor cell clusters.

Lung Metastasis Formation Is Driven by a Pre-Existing Subpopulation of Plakoglobin-Expressing Tumor Cell Clusters With Invasive Properties

Epithelial cell–cell contacts are mediated by distinct adhesion complexes. RNA sequencing data of primary cecum tumors were used to determine expression of gene sets encoding these complexes. Expression of the desmosome signature was most significantly different between lung metastasis–competent and lung metastasis–incompetent PDOs (Figure 4A and Supplementary Figure 5). The desmosome genes DSG3, PKP2, JUP, KLHL24, and DSC2 were most significantly differentially expressed between lung metastasis–competent and lung metastasis–incompetent PDOs (Figure 4B). Among these genes, JUP (encoding plakoglobin) was highly expressed in tumors of a large human CRC cohort[28] (Figure 4C) and was associated with a significantly reduced distant metastasis–free survival (P = .018) (Figure 4D and Supplementary Figure 6). Western blotting showed high expression of plakoglobin in PDO2 and PDO3, but not in PDO1 (Figure 4E). IHC analysis of primary PDO3 tumors showed that plakoglobin expression was restricted to tumor cell clusters

residing within lymphatic vessels (Figure 4F, Supplementary Figure 7). Strikingly, plakoglobin was highly expressed in all lung metastases, but was undetectable in liver metastases in the same mice (Figure 4F and G). Individual lung metastases consisted of plakoglobin-expressing cells (70%–100%) and nonexpressing cells (0%–30%).

The heterogeneous expression of plakoglobin within primary tumors and between metastatic sites indicated that plakoglobin expression may mark distinct pre-existing cell populations within PDO3. Indeed, single-cell messenger RNA sequencing of PDO3 (Supplementary Figure 8A) identified distinct groups of JUP-negative and JUP-positive cells (Figure 4H). Junction signature scores were significantly higher in JUP-positive cells compared with JUP-negative cells (Supplementary Figure 8B). Differential gene expression analysis identified 12 genes that were significantly co-expressed with JUP (Figure 4I, Supplementary Table 3). In a Drosophila model of intestinal cancer, invasion and metastasis are driven by tumor cell clusters that are characterized by a partial epithelial-to-mesenchymal transition (EMT).[29] Therefore, we analyzed JUP expression in relation to signatures marking tumor cell clusters[26] and EMT.[30] JUP co-expressed genes correlated extremely well with both signatures ($R = .65$, $P = 1.2^{e-41}$ and $R = .73$, $P = 1.0^{e-56}$, respectively) (Figure 4J). PDO3, therefore, contains a subpopulation of plakoglobin-expressing cell clusters that is characterized by partial EMT.

Plakoglobin Is Required for Lymphatic Vessel Invasion by Tumor Cell Clusters and for Lung Metastasis Formation

The above data indicate that plakoglobin may play a role in determining lung metastasis competence. To test this, we generated CRISPR-Cas9–mediated JUP knockout variants in PDO2 using 2 distinct guide RNAs targeting exon 2 or 3 (Figure 5A and B). JUP knockout caused a marked "loosening" of the structure of growing organoids, but had no effect on their growth rate or clone-forming capacity (Figure 5C and D). Next, we assessed the effect of JUP knockout on primary tumor formation and metastasis by transplanting PDO2-WT, JUP-KO1, or JUP-KO2 into the cecum of NSG mice. From 25 days onward, mice transplanted with PDO2-WT started to lose weight rapidly. This was not observed in mice transplanted with JUP-KO1 and JUP-KO2 (Figure 5E). All mice were sacrificed 40 days after transplantation when mice with PDO2-WT tumors started to suffer from dyspnea and had reached the humane end point. The lungs in mice with PDO2-WT tumors were significantly heavier compared with the lungs from mice with JUP-KO tumors (Figure 5F). IHC using antibodies recognizing human nucleoli, plakoglobin, and LYVE1 was performed to analyze primary tumor size, invasion into lymphatic vessels, and metastasis formation, in relation to plakoglobin expression (Figure 5G). JUP knockout did not alter primary tumor size (Figure 5H). Plakoglobin expression was significantly lower in JUP-KO tumors, although regions of plakoglobin-positive tumor cells were still detected. Thus, JUP knockout was unsuccessful in a small percentage of the transduced cells, yielding hybrid tumors consisting of plakoglobin-positive
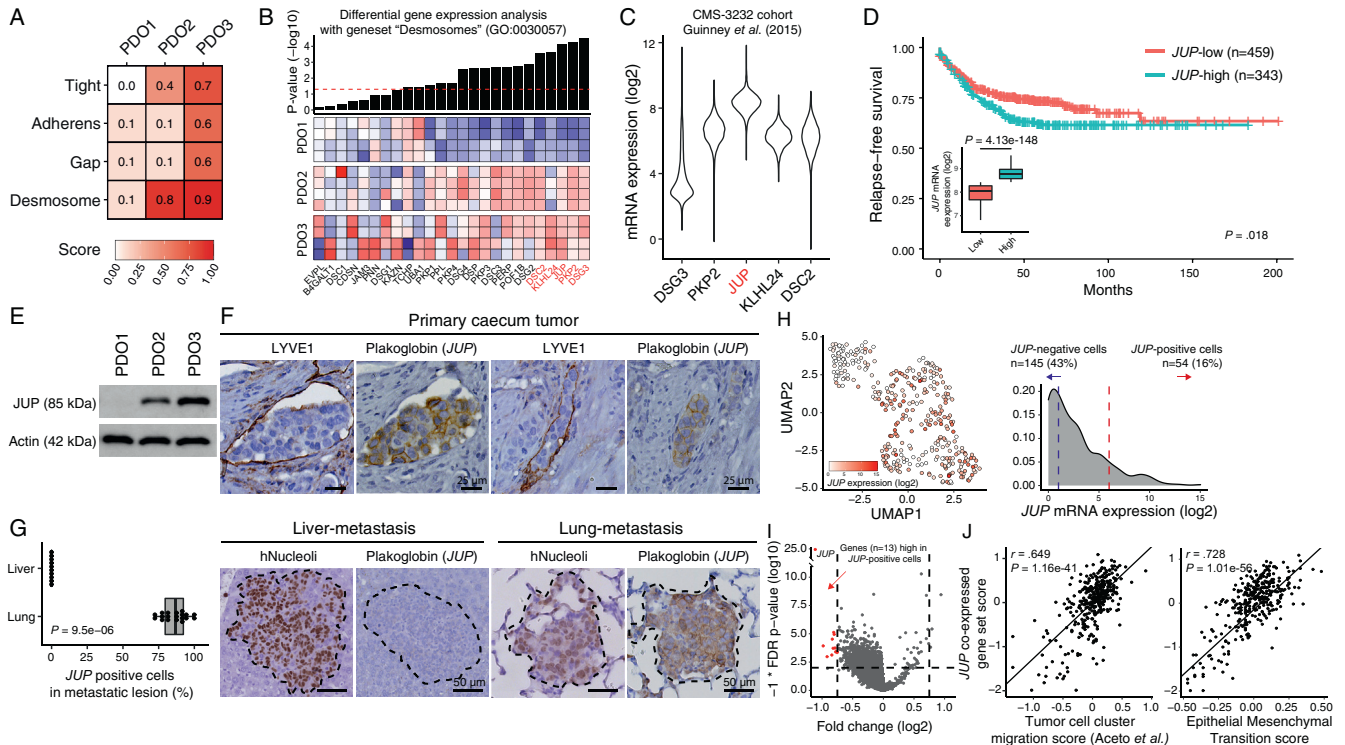
Figure 4. Plakoglobin expression identifies a subgroup of pre-existing lung metastasis-competent tumor cells. (*A*) *Heatmap* represent the mean *z* score values over genes within the following junction gene sets "tight," "adheren," "gap," and "desmosome" (Gene Ontology IDs: 0070160, 0005912, 0005921, and 0030057) in transcriptome data of PDO1, PDO2, and PDO3 primary cecum tumors. (*B*) Differential gene expression analysis of 25 genes in the "desmosome" signature. Genes are ranked based on *P* value (-log10 scaled). *Blue* and *red colors* represent low and high expression, respectively. (*C*) *Violin plot* represent the messenger RNA (mRNA) expression (log2-transformed RPM) of top 5 significantly differentially expressed genes in a large CRC cohort (n = 3232 tumors).[28] (*D*) *Box plot* represent mRNA expression (log2) of *JUP* in the CMS-3232 transcriptome cohort.[28] Low- and high-expression groups are defined by the R2 function "Kaplan Meier" with cutoff mode parameter "average." Relapse-free survival in low (*red*) and high groups (*blue*). Two-sided log-rank test was applied. (*E*) Western blot analysis representing JUP protein presence in the PDO models. (*F*) *Histologic images* of *JUP*-positive cells in primary cecum tumor, liver, and lung metastases in PDO3 model. (*G*) *Box plot* represents the percentage of cells that are *JUP*-positive in a given metastatic lesion (n = 4 mice). (*H*) *Uniform Manifold Approximation and Projection plot* of 336 PDO3 single cells, highlighted by *JUP* mRNA expression (log2-scaled). *Density plot* represents *JUP* mRNA expression (log2-scaled). Expression values of ≤1 and ≥6 indicate *JUP*-negative- and *JUP*-positive cells, respectively. (*I*) *Volcano plot* of all genes representing statistical enrichment of 12 genes ("*JUP* co-expressed geneset") in *JUP*-positive cells (n = 54) compared with *JUP*-negative cells (n = 145). (*J*) *Scatter plot* represents the correlation of "JUP co-expressed gene-set" with the "tumor cell cluster migration gene-set"[26] and "epithelial mesenchymal transition gene-set."[30]

and -negative cells. The number of tumor cell clusters was significantly reduced in *JUP*-KO primary tumors (Figure 5*G* and *H* and Supplementary Figure 9*A*). Notably, in *JUP*-KO tumors, all tumor cell clusters within lymphatic vessels contained cells that had retained plakoglobin expression (Figure 5*G*). *JUP*-KO caused a 50% reduction in lung metastasis formation (Figure 5*I* and *J* and Supplementary Figure 9*B*). All lung metastases in mice bearing *JUP*-KO1 and KO2 tumors contained >50% plakoglobin-expressing cells (Figure 5*K*).

Therapeutic Targeting of the Lymphatic Vasculature Reduces Lung Metastasis Formation

Next, we analyzed whether therapeutic targeting of lymphatic dissemination could reduce lung metastasis. To this end, we generated cohorts of mice carrying PDO2 cecum tumors and treated them with saline or mF4-31C1, an antibody targeting mouse VEGFR3[24,31] (Figure 6*A*). There was no significant difference in body weight loss over

time between the 2 groups (Figure 6*B*). However, the lungs from control mice were significantly heavier compared with the lungs from anti-VEGFR3–treated mice (Figure 6*C*). IHC revealed that anti-VEGFR3 therapy resulted in a significant decrease of lymphatic vessels within the primary tumor. Furthermore, anti-VEGFR3 treatment reduced primary tumor size and caused a highly significant reduction of lung metastasis formation (Figure 6*D*–*F* and Supplementary Figure 10). Finally, we observed a significant correlation between the extent of LYVE1 staining in primary tumors and degree of lung metastasis formation (r = .66, P = .006) (Figure 6*G*).

Lymphatic Invasion by Plakoglobin-Expressing Tumor Cell Clusters in Patients With Lung Metastases

The above results demonstrate that lymphatic invasion by tumor cell clusters in the primary tumor is a major route

toward lung metastasis formation in mice, bypassing the portal circulation and the liver. To corroborate our findings obtained in the PDO models in human cancer, we first analyzed plakoglobin (*JUP*) expression in publicly available

transcriptome data sets from multiple cancer types in The Cancer Genome Atlas.[32] This showed that colon, rectum, stomach, and esophageal cancers are among the tumor types with the highest *JUP* expression (Figure 7A). Second,
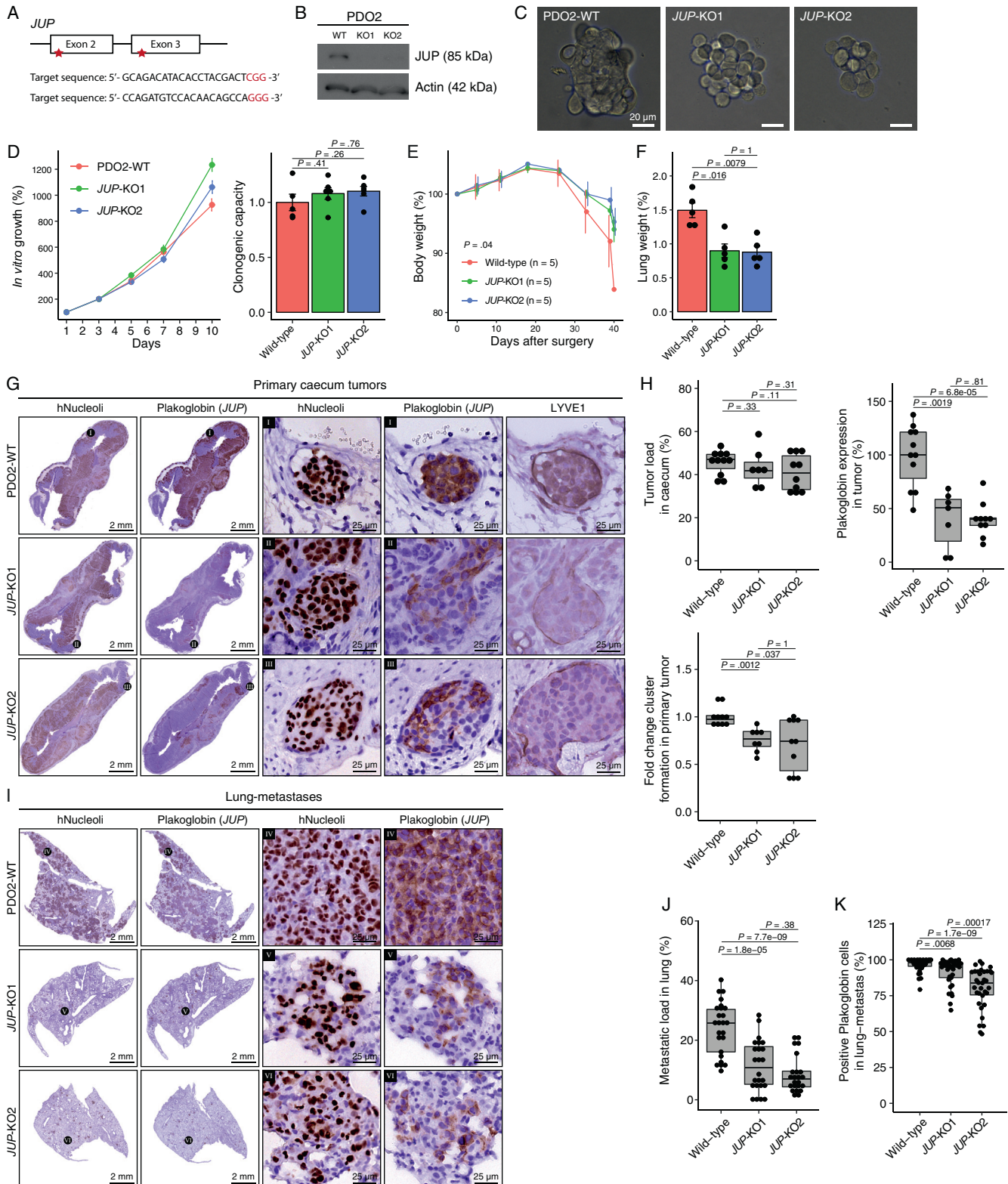
we investigated whether *JUP* expression correlates with lung metastasis incidence across human cancer types.[33] Indeed, *JUP* expression significantly correlated with the incidence of synchronous lung metastasis formation ($P = .006$, $R = .53$) (Figure 7*B*). Third, we investigated a possible correlation of *JUP* expression with overall survival in gastric and esophageal cancer using the publicly available data set described in Ooi et al.[34] Similar to the results in colon cancer (Figure 4*D*), this analysis revealed that high *JUP* expression is also significantly associated with poor overall survival in gastric and esophageal cancers ($P = .015$; Figure 7*C*).

Next, we assembled a composite cohort of human cancer tissues composed of primary colorectal tumors with (n = 12) or without (n = 12) lung metastases (Supplementary Table 4) and primary gastric or esophageal tumors with (n = 10) or without (n = 8) lung metastases (Supplementary Table 5). Thus, in total, we analyzed 42 gastrointestinal cancer cases with (n = 22) or without (n = 20) lung metastases. In this composite cohort, as well as in both cohorts analyzed separately, N-stage was significantly associated with lung metastasis formation (Figure 7*D* and Supplementary Figure 11*A*). We used this cohort to analyze plakoglobin expression by IHC. Plakoglobin expression was scored as weak (score 0), intermediate (score 1), or high (score 2) by an experienced pathologist blinded to the cancer cases (Supplementary Figure 12*A*). Global plakoglobin expression in whole tumor sections was not significantly different among tumors from different locations, tumors that metastasized to the lungs or not, or primary tumors with different N-stages (Supplementary Figure 12*B* and *C*).

Our analysis of the PDO mouse models demonstrates that intra-lymphatic clusters with high plakoglobin expression are the instigators of lung metastasis. To study such clusters in human cancer, we performed IHC on tissue sections of the entire human gastrointestinal cancer cohort (N = 42) using anti–pan-cytokeratin (detecting tumor cells) and anti-podoplanin (detecting lymphatic vessels) (Figure 7*E* and *F*). This analysis revealed that the number of intra-lymphatic tumor cell clusters was significantly correlated with plakoglobin expression, in both the composite cohort (Figure 7*G*) and the CRC cohort analyzed separately (Supplementary Figure 12*D*). In the gastroesophageal cohort, a similar trend was observed, but this did not reach statistical significance, presumably due to the low numbers

(Supplementary Figure 12*D*). Moreover, the presence of intra-lymphatic tumor cell clusters showed a near-significant correlation with the presence of lung metastases in the composite gastrointestinal cohort (Figure 7*H*), which was significant when analyzing the colorectal cohort separately, but not in the gastroesophageal cohort (Supplementary Figure 11*B*).

Finally, in the mouse model, we observed higher expression of plakoglobin in intra-lymphatic tumor cell clusters compared with expression in the (noninvasive) tumor bulk (Figure 4*F* and Supplementary Figure 7). Likewise, we found that, in the human gastrointestinal cancer cohort, lymphatic intravascular tumor cell clusters displayed significantly higher plakoglobin expression, predominantly located at cell–cell contacts compared with nearby noninvading tumor cells in which staining was markedly lower and more diffuse ($P = 7.6^{e-8}$) (Figure 7*I* and *J* and Supplementary Figure 13).

Discussion

In this study, we generated mouse models for metastatic colon cancer with different seeding patterns. Lung metastases were initiated by means of lymphatic invasion of plakoglobin-expressing tumor cell clusters. Likewise, intra-lymphatic clusters of plakoglobin-expressing tumor cells were also found in the primary tumors of patients with lung metastases derived from colon, gastric, or esophageal cancers. Plakoglobin-dependent tumor clusters travel through the mesenteric lymphatic vasculature toward the thoracic duct to reach the lung microvasculature via the subclavian vein and the pulmonary artery. The delineated lymphatic–lung metastasis pathway suggests that, in patients with cancer, lymph node metastases may seed lung metastases. Indeed, the presence of lymph node metastases at initial colon cancer diagnosis predicts extrahepatic recurrence and poor survival in patients undergoing partial hepatectomy for liver metastases.[35] Furthermore, experimental evidence supports the concept of lymph node metastases acting as a source for tumor cells seeding distant metastases.[13,14] However, in most cases (65%), lymph node metastases do not seed distant liver metastases in CRC.[15] Genetic analysis of patient-derived lymph node metastases has demonstrated the polyclonal nature of such lesions,[25,36,37] similar

---

Figure 5. Plakoglobin is required for lymphatic invasion and lung metastasis formation. (*A*) Schematic overview of CRISPR-Cas9–mediated *JUP* gene knockout in PDO2. Two designed single-guide RNA target exon 2 and 3. (*B*) Western blot analysis for plakoglobin presence in PDO2, *JUP*-KO1, and *JUP*-KO2. (*C*) *Brightfield images* represent disrupted cell–cell contact upon *JUP* knockout. (*D*) In vitro growth rate for PDO2, *JUP*-KO1, and *JUP*-KO2. Single cells (n = 10,000) are cultured and viable cells are measured on a given day by CellTiter-Glo 3D Cell Viability Assay (Promega). Regenerative capacity of PDOs was assessed by counting the number of organoids after 2 weeks of culturing 1000 single cells. At least 2 independent experiments with 3 technical replicates. An unpaired *t* test was applied to assess the significance between the groups. (*E*) Body weight of NSG mice cecum-implanted with PDO2, *JUP*-KO1, or *JUP*-KO2 (n = 5 mice per group). Analysis of variance test was applied to assess the significance of weight difference on day 40 between the groups. (*F*) Lung weights (percentage of total body weight) on observed end point (day 40) of experiment. (*G*) Representative hNucleoli, plakoglobin, and LYVE1 staining for primary cecum tumor. (*H*) *Box plots* represent tumor load (%) in cecum tissue, plakoglobin expression (%) in tumor tissue, and fold-change tumor cell cluster formation in cecum tissue. (*I*) Representative hNucleoli and plakoglobin staining for lung tissues. (*J*) Metastatic tumor load in lung, measured by percentage of hNucleoli staining relative to healthy lung tissue. (*K*) Quantification of *JUP*-positive cell detection in lung-metastatic lesions. Mann-Whitney U test was applied.
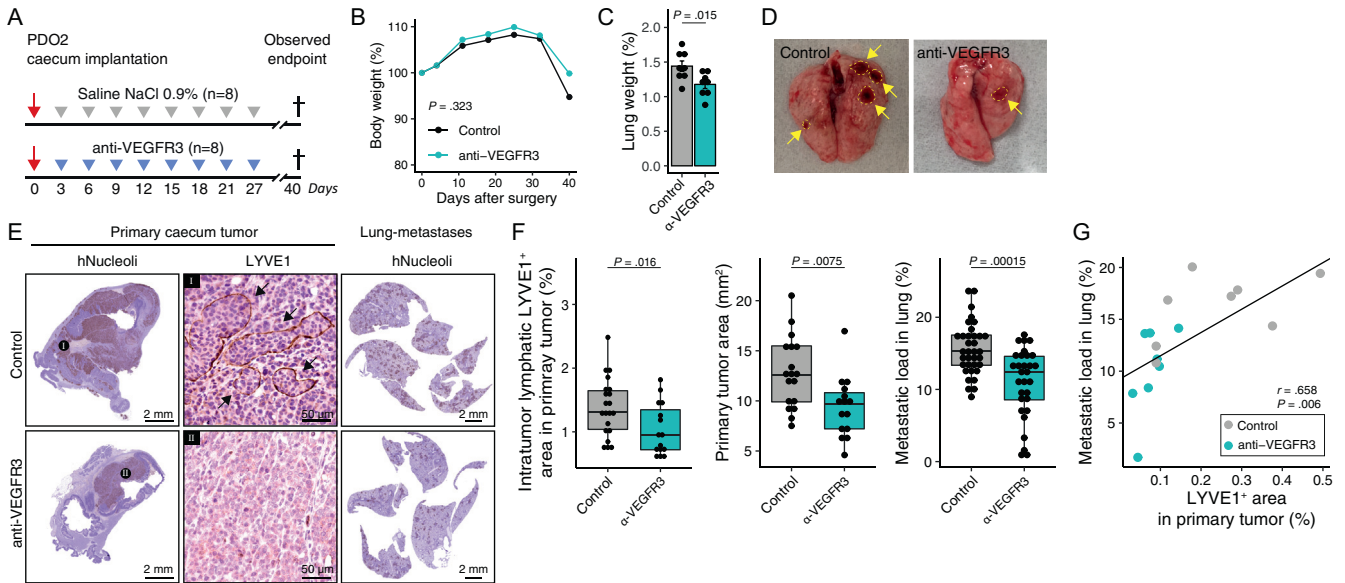
Figure 6. Inhibition of lymphangiogenesis reduces lung metastasis formation. (*A*) Experimental protocol of intraperitoneal injection (100 μL) treatment with saline (NaCl; 0.9%) or mF4-31C1 (anti-VEGFR3; 625 μg), starting post 3 day's orthotopic cecum implantation with 3-day interval. n = 8 mice per group. (*B*) Mice body weight relative to day 0 (start of experiment). All animals are sacrificed at the first observed end point of control mice (day 40). Analysis of variance test was applied. (*C*) Lung weights (percentage of total body weight) on day 40. (*D*) Representative macroscopic lung images of control (*left*) and anti-VEGFR3–treated (*right*) mice. *Arrows* indicate unhealthy spots. (*E*) Histologic hNucleoli and LYVE1 staining in primary cecum tumor and lungs of control and anti-VEGFR3–treated mice. (*F*) *Box plots* represent LYVE1 area (mm^2), primary tumor area (mm^2), and metastatic load, as measured by percentage of hNucleoli staining relative to healthy lung tissue. (*G*) *Scatter plots* represent correlation of LYVE1$^+$ area in primary cecum tumor with lung metastatic load. *Dot* represents a given mouse.

to the lung metastases in our study. Importantly, we found no selection against any of the clones present within the primary tumors. The low selection pressure may be explained in part by the finding that metastasis-incompetent cells are carried over to the lungs by competent cells in hybrid/oligoclonal tumor cell clusters. In general, tumor cell clusters tend to be more potent instigators of metastasis than single cells in different model systems for various cancer types.[26,38–50] Multiple factors are likely to contribute to the enhanced metastatic potential of tumor cell clusters, including increased survival signaling by cell–cell contacts; increased resistance to immune cells; and functional cooperation by distinct, phenotypically stable, cell types during outgrowth.[51] We identified *JUP*, encoding the desmosome protein plakoglobin, as an essential gene defining lung metastasis competence. Invasion-competent plakoglobin-expressing cell clusters were characterized by a partial EMT phenotype in which cell–cell contacts were maintained and mesenchymal features were acquired. Partial EMT can drive invasion and metastasis initiation by tumor cell clusters in a *Drosophila* model of intestinal cancer.[29] An important consequence of the "hitchhike" model is that genetic analysis of lung metastases at the single-cell level may not necessarily identify features driving lung metastasis competence, as subpopulations of these cells may be metastasis-incompetent. We propose that lymphatic invasion by polyclonal tumor cell clusters is a major cause of the polyclonal nature of lymph node metastases[25,36] and lung metastases (this study). In this respect, it is important to

note that in the PDO mouse models, tumors grow and metastasize in a relatively short period of time (weeks), and can take years in patients with cancer. Therefore, local organ-specific and time-dependent processes may influence progressive genetic evolution of distant metastases growing in patients with cancer.

The plakoglobin–lymphatic–lung metastasis route identified here should now be confirmed through pairwise genetic analysis of lymph node metastases and lung metastases from patients with cancer. If this can indeed be demonstrated, it would reinforce the importance of extensive lymph node dissection during surgical removal of the primary tumor, as is advised in oncologic treatment guidelines. An additional potential route to lung metastasis formation is "onward metastasis" initiated by previously established liver metastases. Indeed, genetic evidence for the existence of a liver–lung metastasis pathway has been provided recently.[10] Whether this is caused by tumor cell invasion into blood or lymphatic vessels is currently unknown.

Our results suggest that genetic variation between liver and lung metastases and among lung metastases in individual patients may be substantial, depending on the anatomic route that caused their seeding. Possibly, this could influence therapy response. Although mutations in oncogenic driver genes tend to be clonal and, therefore, homogeneous among lesions in individual patients,[52] these do not predict response to systemic chemotherapy. Moreover, clonal driver mutations cannot account for the
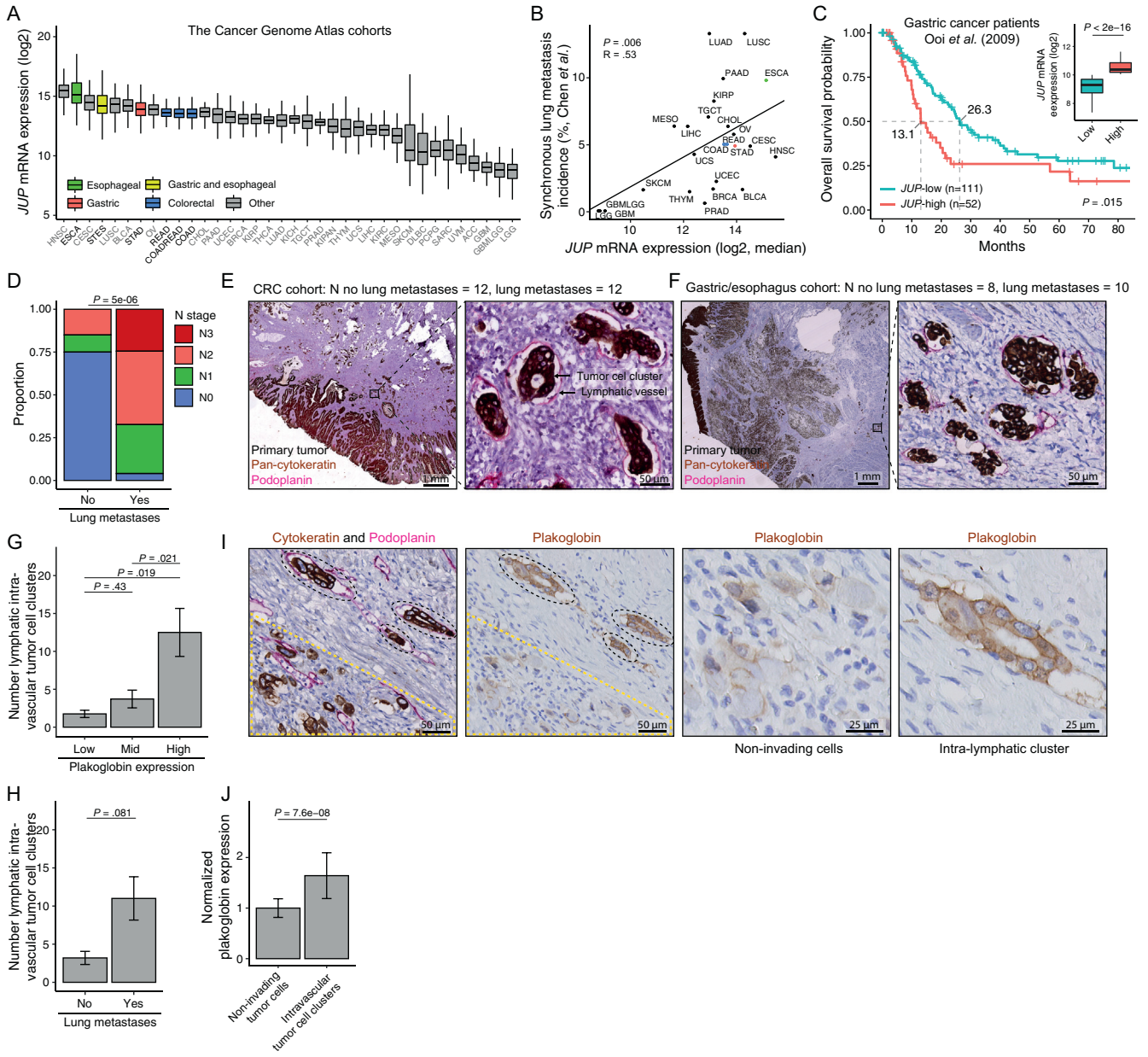
Figure 7. Increased lymphatic invasion by plakoglobin-expressing tumor cell clusters and lymph node metastasis formation in patients with lung metastases. (*A*) *JUP* messenger RNA (mRNA) expression (log2) in The Cancer Genome Atlas (TCGA) cohorts.[32] (*B*) *Correlation plot* showing median *JUP* mRNA expression (log2) values in the TCGA cohorts vs the percentage of synchronous lung metastasis incidence, reported in Chen et al.[33] (*C*) *Box plot* representing mRNA expression (log2) of *JUP* in a gastric cancer transcriptome cohort.[34] Low- and high-expression groups are defined by the R2 function "Kaplan Meier" with expression cutoff mode parameter "average." The *Kaplan-Meier plot* shows overall survival in the *JUP*-low (*blue*) and *JUP*-high subgroups (*red*). Mann-Whitney U test and 2-sided log-rank test were applied. (*D*) *Stacked bar plot* representing the frequency of N stages (N0, N1, N2, N3) in the composite gastrointestinal cohort comparing patients with lung metastases (n = 22) with those without lung metastases (n = 20). Fisher exact test was applied. (*E*) Histologic co-staining of pan-cytokeratin (*brown*) and podoplanin (*pink*) in human colon and (*F*) gastric resection specimens, showing intra-lymphatic tumor cell clusters. (*G*) *Bar plot* representing the mean of lymphatic intravascular tumor cell clusters in plakoglobin-low, -mid, and -high tumors in the composite gastrointestinal cohort. Mann-Whitney U test was applied. (*H*) *Bar plot* representing the mean of lymphatic intravascular tumor cell clusters in the composite gastrointestinal cohort comparing patients with or without lung metastases. Mann-Whitney U test was applied. (*I*) Histologic co-staining (*left*) of pan-cytokeratin (*brown*), podoplanin (*pink*), and plakoglobin (*brown*). *Dashed black ellipses* represent intra-lymphatic tumor cell clusters. *Yellow dashed triangles* indicate areas containing noninvading tumor cells only. (*J*) *Bar plot* representing the mean of normalized plakoglobin expression in intra-lymphatic tumor cell clusters compared with noninvading tumor cells. Mann-Whitney U test was applied.

heterogeneous responses that are frequently observed in individual patients. Possibly, nondriver subclonal genetic heterogeneity (this study), epigenetic processes, and/or gene expression–based phenotypic diversity may play important roles in determining therapy response.

In conclusion, our study identified plakoglobin-expressing tumor cell clusters entering the lymphatic vasculature as instigators of lung metastasis formation. The cooperative nature of this process underlies the polyclonal nature of the resulting lung metastases and may contribute to the low clonal selection pressure. The findings reinforce the importance of extensive lymph node dissection during surgical removal of the primary tumor and may be relevant for interpreting heterogeneous responses to systemic therapy. Finally, therapeutic targeting of the plakoglobin–lymphatic–lung metastasis pathway could help block systemic spread during neoadjuvant treatment before colon tumor resection, and/or in patients with inoperable primary tumors.

Supplementary Material

Note: To access the supplementary material accompanying this article, visit the online version of *Gastroenterology* at www.gastrojournal.org, and at https://doi.org/10.1053/j.gastro.2023.02.047.

References

1. Riihimaki M, Hemminki A, Sundquist J, et al. Patterns of metastasis in colon and rectal cancer. Sci Rep 2016;6: 29765.
2. Petrowsky H, Fritsch R, Guckenberger M, et al. Modern therapeutic approaches for the treatment of malignant liver tumours. Nat Rev Gastroenterol Hepatol 2020; 17:755–772.
3. Mitry E, Guiu B, Cosconea S, et al. Epidemiology, management and prognosis of colorectal cancer with lung metastases: a 30-year population-based study. Gut 2010;59:1383–1388.
4. Stewart CL, Warner S, Ito K, et al. Cytoreduction for colorectal metastases: liver, lung, peritoneum, lymph nodes, bone, brain. When does it palliate, prolong survival, and potentially cure? Curr Probl Surg 2018; 55:330–379.
5. Kanemitsu Y, Shimizu Y, Mizusawa J, et al. Hepatectomy followed by mFOLFOX6 versus hepatectomy alone for liver-only metastatic colorectal cancer (JCOG0603): a phase II or III randomized controlled trial. J Clin Oncol 2021;39:3789–3799.
6. Obenauf AC, Massagué J. Surviving at a distance: organ-specific metastasis. Trends Cancer 2015; 1:76–91.
7. Jiao LR, Apostolopoulos C, Jacob J, et al. Unique localization of circulating tumor cells in patients with hepatic metastases. J Clin Oncol 2009;27: 6160–6165.
8. Wind J, Tuynman JB, Tibbe AG, et al. Circulating tumour cells during laparoscopic and open surgery for primary colonic cancer in portal and peripheral blood. Eur J Surg Oncol 2009;35:942–950.
9. Rahbari NN, Bork U, Scholch S, et al. Metastatic spread emerging from liver metastases of colorectal cancer: does the seed leave the soil again? Ann Surg 2016; 263:345–352.
10. **Chen HN, Shu Y, Liao F**, et al. Genomic evolution and diverse models of systemic metastases in colorectal cancer. Gut 2021;71:322–332.
11. Tan KK, Lopes Gde L Jr, Sim R. How uncommon are isolated lung metastases in colorectal cancer? A review from database of 754 patients over 4 years. J Gastrointest Surg 2009;13:642–648.
12. Zhang N, Di J, Wang Z, et al. Genomic profiling of colorectal cancer with isolated lung metastasis. Cancer Cell Int 2020;20:281.
13. Pereira ER, Kedrin D, Seano G, et al. Lymph node metastases can invade local blood vessels, exit the node, and colonize distant organs in mice. Science 2018; 359:1403–1407.
14. Brown M, Assen FP, Leithner A, et al. Lymph node blood vessels provide exit routes for metastatic tumor cell dissemination in mice. Science 2018;359: 1408–1411.
15. Naxerova K, Reiter JG, Brachtel E, et al. Origins of lymphatic and distant metastases in human colorectal cancer. Science 2017;357:55–60.
16. Kasashima H, Duran A, Cid-Diaz T, et al. An orthotopic implantation mouse model of hepatocellular carcinoma with underlying liver steatosis. STAR Protoc 2020;1: 100185.
17. **Calon A, Espinet E**, Palomo-Ponce S, et al. Dependency of colorectal cancer on a TGF-beta-driven program in stromal cells for metastasis initiation. Cancer Cell 2012; 22:571–584.
18. Lau HCH, Kranenburg O, Xiao H, et al. Organoid models of gastrointestinal cancers in basic and translational research. Nat Rev Gastroenterol Hepatol 2020; 17:203–222.
19. Sato T, Stange DE, Ferrante M, et al. Long-term expansion of epithelial organoids from human colon, adenoma, adenocarcinoma, and Barrett's epithelium. Gastroenterology 2011;141:1762–1772.
20. Sato T, Vries RG, Snippert HJ, et al. Single Lgr5 stem cells build crypt-villus structures in vitro without a mesenchymal niche. Nature 2009;459:262–265.
21. **Küçükköse E, Wensink GE**, Roelse CM, et al. Mismatch repair status in patient-derived colorectal cancer organoids does not affect intrinsic tumor cell sensitivity to systemic therapy. Cancers (Basel) 2021; 13:5434.
22. Weber K, Thomaschewski M, Benten D, et al. RGB marking with lentiviral vectors for multicolor clonal cell tracking. Nat Protoc 2012;7:839–849.
23. Fumagalli A, Suijkerbuijk SJE, Begthel H, et al. A surgical orthotopic organoid transplantation approach in mice to visualize and study colorectal cancer progression. Nat Protoc 2018;13:235–247.
24. Pytowski B, Goldman J, Persaud K, et al. Complete and specific inhibition of adult lymphatic regeneration by a

novel VEGFR-3 neutralizing antibody. J Natl Cancer Inst 2005;97:14–21.

25. Reiter JG, Hung WT, Lee IH, et al. Lymph node metastases develop through a wider evolutionary bottleneck than distant metastases. Nat Genet 2020; 52:692–700.

26. Aceto N, Bardia A, Miyamoto DT, et al. Circulating tumor cell clusters are oligoclonal precursors of breast cancer metastasis. Cell 2014;158:1110–1122.

27. Frenkel N, Poghosyan S, Alarcon CR, et al. Long-lived human lymphatic endothelial cells to study lymphatic biology and lymphatic vessel/tumor coculture in a 3D Microfluidic Model. ACS Biomater Sci Eng 2021; 7:3030–3042.

28. **Guinney J, Dienstmann R, Wang X**, et al. The consensus molecular subtypes of colorectal cancer. Nat Med 2015;21:1350–1356.

29. **Campbell K, Rossi F**, Adams J, et al. Collective cell migration and metastases induced by an epithelial-to-mesenchymal transition in *Drosophila* intestinal tumors. Nat Commun 2019;10:2311.

30. Liberzon A, Birger C, Thorvaldsdottir H, et al. The Molecular Signatures Database (MSigDB) hallmark gene set collection. Cell Syst 2015;1:417–425.

31. **Hoshida T, Isaka N**, Hagendoorn J, et al. Imaging steps of lymphatic metastasis reveals that vascular endothelial growth factor-C increases metastasis by increasing delivery of cancer cells to lymph nodes: therapeutic implications. Cancer Res 2006;66:8065–8075.

32. Weinstein JN, Collisson EA, Mills GB, et al. The Cancer Genome Atlas Pan-Cancer analysis project. Nat Genet 2013;45:1113–1120.

33. Chen H, Stoltzfus KC, Lehrer EJ, et al. The epidemiology of lung metastases. Front Med (Lausanne) 2021;8: 723396.

34. Ooi CH, Ivanova T, Wu J, et al. Oncogenic pathway combinations predict clinical prognosis in gastric cancer. PLOS Genetics 2009;5:e1000676.

35. Buisman FE, Giardiello D, Kemeny NE, et al. Predicting 10-year survival after resection of colorectal liver metastases; an international study including biomarkers and perioperative treatment. Eur J Cancer 2022;168:25–33.

36. Ulintz PJ, Greenson JK, Wu R, et al. Lymph node metastases in colon cancer are polyclonal. Clin Cancer Res 2018;24:2214–2224.

37. Hu Z, **Ding J, Ma Z**, et al. Quantitative evidence for early metastatic seeding in colorectal cancer. Nat Genet 2019; 51:1113–1122.

38. Allen TA, Asad D, Amu E, et al. Circulating tumor cells exit circulation while maintaining multicellularity, augmenting metastatic potential. J Cell Sci 2019; 132:jcs231563.

39. Watanabe S. The metastasizability of tumor cells. Cancer 1954;7:215–223.

40. Fidler IJ. The relationship of embolic homogeneity, number, size and viability to the incidence of experimental metastasis. Eur J Cancer (1965) 1973;9:223–227.

41. Liotta LA, Saidel MG, Kleinerman J. The significance of hematogenous tumor cell clumps in the metastatic process. Cancer Res 1976;36:889–894.

42. Zajac O, Raingeaud J, Libanje F, et al. Tumour spheres with inverted polarity drive the formation of peritoneal metastases in patients with hypermethylated colorectal carcinomas. Nat Cell Biol 2018;20:296–306.

43. Liu X, Taftaf R, Kawaguchi M, et al. Homophilic CD44 interactions mediate tumor cell aggregation and polyclonal metastasis in patient-derived breast cancer models. Cancer Discov 2019;9:96–113.

44. Lo HC, Xu Z, Kim IS, et al. Resistance to natural killer cell immunosurveillance confers a selective advantage to polyclonal metastasis. Nat Cancer 2020;1:709–722.

45. Wrenn ED, Yamamoto A, Moore BM, et al. Regulation of collective metastasis by nanolumenal signaling. Cell 2020;183:395–410.e19.

46. Maddipati R, Stanger BZ. Pancreatic cancer metastases harbor evidence of polyclonality. Cancer Discov 2015; 5:1086–1097.

47. Cheung KJ, Ewald AJ. A collective route to metastasis: seeding by tumor cell clusters. Science 2016; 352:167–169.

48. Cheung KJ, Padmanaban V, Silvestri V, et al. Polyclonal breast cancer metastases arise from collective dissemination of keratin 14-expressing tumor cell clusters. Proc Natl Acad Sci U S A 2016;113:E854–E863.

49. Campbell NR, Rao A, Hunter MV, et al. Cooperation between melanoma cell states promotes metastasis through heterotypic cluster formation. Dev Cell 2021; 56:2808–2825.e10.

50. Tiede S, Kalathur RKR, Lüönd F, et al. Multi-color clonal tracking reveals intra-stage proliferative heterogeneity during mammary tumor progression. Oncogene 2021;40:12–27.

51. Wrenn E, Huang Y, Cheung K. Collective metastasis: coordinating the multicellular voyage. Clin Exp Metastasis 2021;38:373–399.

52. **Reiter JG, Makohon-Moore AP, Gerold JM**, et al. Minimal functional driver gene heterogeneity among untreated metastases. Science 2018;361:1033–1037.

Correspondence
Address correspondence to: Onno Kranenburg, PhD, Department of Imaging and Cancer, University Medical Center Utrecht, Heidelberglaan 100, PO Box 85500, Utrecht, 3584 CX, The Netherlands. e-mail: o.kranenburg@umcutrecht.nl.

GI CANCER

Kristiaan J. Lenos, PhD (Resources: Supporting).

Louis Vermeulen, PhD, MD (Resources: Supporting).

Miriam Koopman, PhD, MD (Resources: Supporting).

Jeanine M. L. Roodhart, PhD, MD (Resources: Supporting).

Geert J. P. L. Kops, PhD (Resources: Supporting).

Inne H. M. Borel Rinkes, PhD, MD (Methodology: Supporting).

Jeroen Hagendoorn, PhD, MD (Methodology: Supporting).

Kamila Naxerova, PhD (Formal analysis: Supporting; Writing – review & editing: Supporting).

Onno Kranenburg, PhD (Conceptualization: Lead; Formal analysis: Lead; Investigation: Lead; Methodology: Lead; Supervision: Lead; Visualization: Lead; Writing – original draft: Lead).

Data Availability
The patient-derived organoids that are described in this study may be obtained through a Material Transfer Agreement. Bulk and single-cell RNA sequencing are accessible on request in the R2: Genomics Analysis and Visualization Platform (http://r2.amc.nl).

Supplementary Materials and Methods

Patient-Derived Tumor Organoid Culture

Organoids were established previously[21] from solid lesions, according to methods described by Fujii et al.[e1] Tissue specimens were cut into small pieces, washed 10 times with cold phosphate-buffered saline (PBS), and digested with 0.1 mg/mL Liberase TH research grade (Roche, Mannheim, Germany, no. 05401135001) for 60 minutes at 37°C, with vortexing every 15 minutes. The cell suspension was collected, centrifuged, and embedded in ice-cold Matrigel Basement Membrane Matrix (Corning) mixed with CRC culture medium (Supplementary Table 1) in a 3:1 ratio. Drops of 10-μL cell suspension were allowed to solidify for 30 minutes in an incubator at 37°C and 5% CO_2, after which they were overlaid with CRC culture medium. Fresh medium was added once to twice per week. Outgrowing organoids were passaged by mechanical and enzymatic disruption with TrypLE Express (Gibco, no. 12604021) for 5–10 minutes at 37°C and replated in a prewarmed 6-well plate. Rho-associated kinase inhibitor Y-27632 (Tocris, no. 1254, 10 μM) was added to culture medium on plating for 2 days.

Tissue Processing and Image Analysis

Mouse organs containing multicolor endogenous fluorescence in tumor/metastases were fixed using 4% paraformaldehyde in PBS solution overnight at 4°C, followed by tissue preservation in a 20% sucrose solution for 12 hours at 4°C. Samples were cut into 4-μm-thick frozen tissue sections and covered with ProLong Gold Antifade Mountant (Thermo Fisher Scientific) to ensure fluorescent signal preservation. For high-resolution imaging, section were scanned with an LSM 700 confocal microscope (Carl Zeiss) using Zen 2016 software. The following settings were used for acquisition: EC Plan-Neofluar 10x/0.30 M27 objective, pinhole 69.18 μm, scaling 1.25 μm/pixel or EC Plan-Neofluar 20x/0.50 M27 objective, pinhole 69.18 μm, and scaling 0.63 μm/pixel.

The raw CZI image files were exported in the OME-TIFF format using Zen 2016 software. Subsequently, the TIFF images were processed using a custom Python (version 3.8.13) script. First, TIFF files were read in using scikit-image (version 0.19.2) and split into the 3 image channels. For images that were acquired with a higher resolution, the image channels were down-sampled using the block_reduce function from the scikit-image package (version 0.19.2) to a final resolution of 1.25 μm/pixel. Subsequently, all images are converted to an 8-bit format and a soft Gaussian filter was applied with a sigma of 0.25 using the scipy-ndimage package (version 1.8.0).

Afterward, for all images and all 3 image channels, autofluorescence of normal tissue was individually contrast-corrected by intensity clipping at appropriate, manually chosen thresholds using a threshold level of at least 1. For this, the clipping value was subtracted from all pixel values in the image, followed by setting 0 as the lowest possible value. Subsequently, the pixel values were rescaled so that 0.6% of pixel values >0 were oversaturated after contrast enhancing (ie, >255 in the rescaled image). Last, the contrast-adjusted image channels were combined and exported as PNG files.

The output images were processed in R (version 4.0.2). For each pixel, the x- and y-coordinates as well as the red, green, and blue (RGB) pixel values were extracted. Pixels with RGB(0,0,0) (ie, white) and RGB(255,255,255) (ie, black) were excluded. Afterward, the pixel colors were converted from an RGB into a Hue Saturation Value scale using the *rgb2hsv* function from the grDevices package and the data tables for each image were exported.

The output files were analyzed in 2 different ways that both rely on the same pre-filtering approach that aims to further reduce the amount of background pixels in the analysis. For this, only pixels in which the sum of the RGB color values was >50 were included in the analysis. In the first approach, the Simpson Diversity Index (SDI) is used to quantify the color diversity. For this, 10 equally sized bins were defined for the calculated hue values that fall into a range of 0° to 360° and the number of pixels corresponding to each bin was counted. These counts were used as "species" sizes to calculate the SDI using the vegan R package. Moreover, if there were multiple images for a specific mouse and organ type, the hue frequencies were first added before calculating the SDI on the combined data in order to estimate whole-organ diversity. This process was repeated 9 times. Each time the start of all bins was shifted by one-tenth of the bin width to reduce bias on where to draw the borders of each bin. Afterward, the mean SDI across all repetitions was calculated. Finally, the data were plotted as *boxplots* for all different organs and significance was tested using the Kruskal-Wallis test. This approach was adapted from the analysis described by Coffey and colleagues.[e2] However, in our approach, equally sized bins were used and bin starts were varied.

Whereas the first approach only considers the color values of the pixels and not their location in the image, the second approach quantifies diversity in a physical distance–based manner by means of comparing the color of pixels at different distances. This allows us to assess diversity across multiple distances and might be informative for intra- as well as inter-lesion heterogeneity. For this, 20,000 pixels are randomly sampled in each image, or fewer, in case the image has fewer pixels than that after filtering for the sum of RGB values, as described above. Afterward, pairwise comparisons between all possible combinations were performed by means of calculating the physical Euclidean distance between the 2 pixels in the image, that is, how far apart the 2 pixels are, and the Euclidean distance between the 2 pixels in the RGB color space, that is, how similar in color the 2 pixels are. The distance in RGB color space is then normalized to the maximum obtainable Euclidean distance in the RGB color space (441.67; comparing [0,0,0] with [255,255,255]). For fixed Euclidean distances given as a threshold, pixels that were at most this distance apart were used to calculate the average normalized Euclidean distance in RGB space to estimate color diversity. This was done for several distances and the whole random sampling process was repeated 9 times, followed by averaging the results of all repetitions. If there were multiple images for a mouse and organ type, the results for these were summarized by

averaging. Afterward, an average of all mice was calculated for the different organ types and the results are plotted as a line.

Immunohistochemistry and Quantification

Human tumor samples and mouse organs containing human tumor were fixed in 4% formaldehyde solution and paraffin-embedded. Sections of 4-μm thickness were made. Before the staining, tissue sections were deparaffinized and rehydrated. Endogenous peroxidase activity was blocked with 1.5% hydrogen peroxide for 30 minutes. Heat-induced antigen retrieval was carried out using citrate buffer (pH 6.0) for 20 minutes, followed by the cooling of tissue sections for 20 minutes. Sections were incubated overnight at 4°C with primary antibodies (Supplementary Table 2) diluted in PBS with 0.1% sodium azide and 3% bovine serum albumin. The next day, sections were washed 3 times with 0.05% Tween-PBS solution for 5 minutes, followed by a 1-hour incubation with the horseradish peroxidase–conjugated secondary antibody. Subsequently, sections were washed 3 times with 1× PBS for 5 minutes and developed with 3,3'-diaminobenzidine (DAB) chromogen for 10 minutes at room temperature in the dark. Sections were rinsed under running tap water for 10 minutes and counterstained with hematoxylin, followed by dehydration and mounting.

Stainings were scanned using NanoZoomerXR whole slide scanner (Hamamatsu) at 40× magnification, with a resolution of 0.25 μm/pixel. Quantification of the scans was performed using QuPath program analysis program.[e3] Target of interest was quantified using QuPath's Trained Pixel classification command that allows automated recognition of background, tissue (hematoxylin), and DAB staining areas. The percentage of target of interest areas was then calculated using the following formula: DAB area / (DAB + tissue– background area) * 100. For quantification of tumor cell cluster numbers, we defined "clusters" as groups of 2–100 tumor cells that are detached from the tumor bulk. Scoring tumors for intravascular tumor cell clusters was performed by a pathologist.

DNA and RNA Isolation

Tumor organoids were grown for 3 days and subsequently starved overnight in Advanced Dulbecco's modified Eagle medium/F12 supplemented with HEPES buffer, penicillin/streptomycin, and GlutaMAX. The organoid cultures were harvested using Dispase in order to remove Matrigel and were lysed in RLT-buffer (Qiagen) supplemented with 1% β- mercaptoethanol. Frozen tumor tissues, including cecum tumor, peritoneal, liver, and lung metastasis, were lysed in the same buffer. Total DNA and/or RNA was isolated using the DNeasy and RNeasy Mini Kit (Qiagen) according to the manufacturer's instructions. Extracted genomic material concentration and quality was measured using NanoDrop 2000 (Thermo Scientific) and Bioanalyzer 2100 (Agilent).

CRISPR-Cas9–Mediated Plakoglobin (JUP) Knockout

Two single-guide RNA targeting exon 2 (5'-GCAGAC ATACACCTACGACTCGG-3') and exon 3 (5'-CCAGATGT

CCACAACAGCCAGGG-3') were ligated into LentiCRISPRv2 (Addgene no. 52961). Lentiviral production was performed using a calcium phosphate transfection protocol in human embryonic kidney 293T cells using the transfer plasmid (15 μg), pMD2.G (Addgene, no. 12259, 7.5 μg), and psPAX2 (Addgene, no. 12260, 7.5 μg). The following day, medium was replaced by advanced Dulbecco's modified Eagle medium/F12 medium (Invitrogen) supplemented with HEPES buffer (Lonza, 10 mM), penicillin/streptomycin (Gibco, 50 U/mL), and GlutaMAX (Gibco, 2 mM). The next day, 50,000 single cells of organoids were resuspended in the virus medium (which was filtered through a 0.45-μm polyethersulfone filter), supplemented with Polybrene (Sigma-Aldrich, 8 μg/mL), N-acetylcysteine (Sigma-Aldrich, 1.25 mM), and Rho-associated kinase inhibitor Y-27632 (Sigma-Aldrich, 10 μM), and incubated overnight 37°C, 5% (vol/vol) CO_2 on nonadherent plates (ultra-low attachment surface, Sigma-Aldrich). After 24-hour incubation, cells were washed twice in PBS (Sigma-Aldrich) and cultured as described above.

Next-Generation Sequencing

Whole-genome sequencing of PDO1–3 organoids was performed on an Illumina NovaSeq 6000 (2 × 150 bp). Bulk RNA sequencing of the tumor organoids and frozen tumor samples was performed on an Illumina NextSeq 500 (1 × 75 bp). Mapping (whole-genome sequencing and RNA), germline SNV + InDel, copy number, and structural-variation calling was performed using the "Illumina Analysis Pipeline" of Utrecht Bioinformatics Expertise Core within the Center for Molecular Medicine at the University Medical Center.

Statistical Analyses

Statistical analysis was performed in the R software, version 4.0.2. Kruskal-Wallis test was used for SDI difference across organs. Unpaired 2-tailed Mann–Whitney–Wilcoxon was used for all histologic analyses. One-way analysis of variance was used for next-generation sequencing analyses. Values are presented as mean ± SEM. $P < .05$ was considered statistically significant.

Supplementary References

e1. Fujii M, Shimokawa M, Date S, et al. A colorectal tumor organoid library demonstrates progressive loss of niche factor requirements during tumorigenesis. Cell Stem Cell 2016;18:827–838.

e2. Coffey SE, Giedt RJ, Weissleder R. Automated analysis of clonal cancer cells by intravital imaging. IntraVital 2013;2(3). https://doi.org/10.4161/intv.26138.

e3. Bankhead P, Loughrey MB, Fernandez JA, et al. QuPath: open source software for digital pathology image analysis. Sci Rep 2017;7:16878.
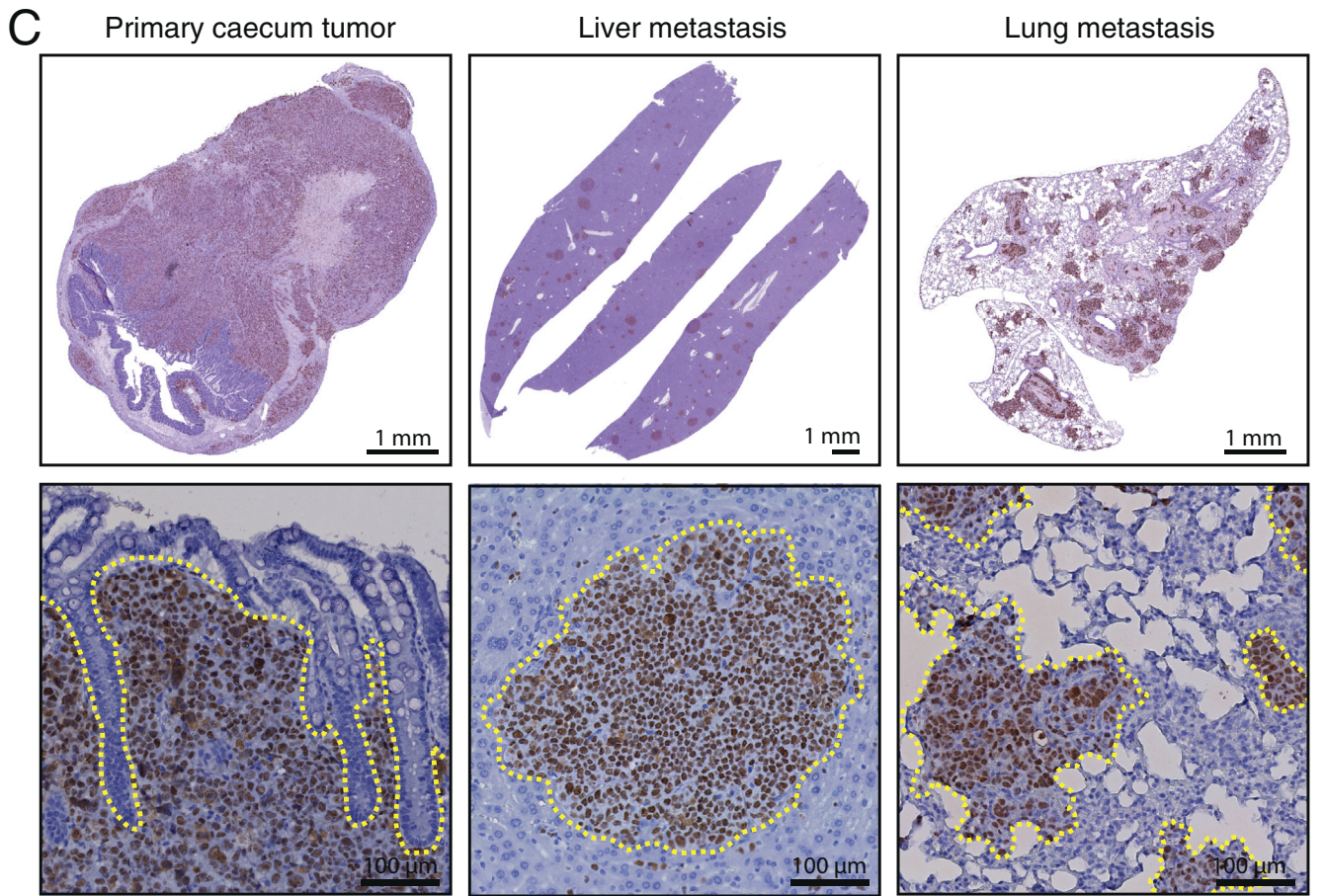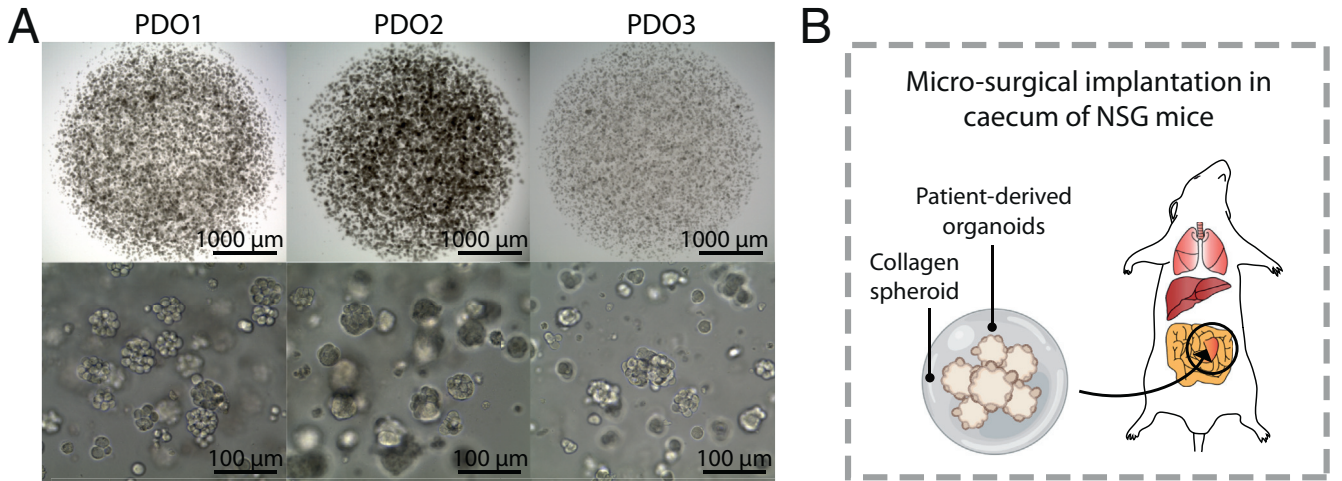
|	Mice with metastasis	Total number of liver-metastasis	Liver-metastasis load (%)	Total number of lung-metastasis	Lung-metastasis load (%)
PDO1	100% (10/10)	6 ± 1	12.3	0	0
PDO2	100% (10/10)	0	0	26.3 ± 9.1	22.4
PDO3	100% (10/10)	33.3 ± 8.1	5.1	31.5 ± 7.8	6.6
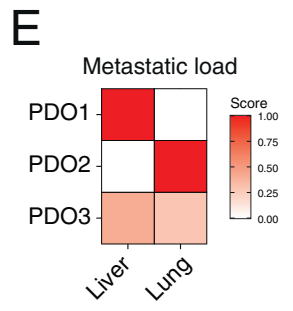
Supplementary Figure 1. Generation of spontaneous CRC metastasis models with distinct organ tropism. (*A*) Microscope bright field *images* of PDOs. *Scale bars:* 100 and 1000 μm. (*B*) Experimental setup of the orthotopic implantation model. PDOs (250,000 cells) are cultured in type 1 collagen and subsequently transplanted under the serosa layer of the cecal wall of immune-deficient mice. (*C*) Representative hNucleoli staining of a primary tumor, liver, and lung metastases. The borders between tumors and healthy tissue are indicated with a *dotted line*. *Scale bars:* 100 μm and 1 mm. (*D*) Liver and lungs were analyzed for presence of spontaneous metastases. The mean number of metastases per mouse and the mean metastatic load relative to normal (liver/lung) tissue are indicated. (*E*) *Heatmap* showing metastatic load in in liver and lung for 3 different PDO models.
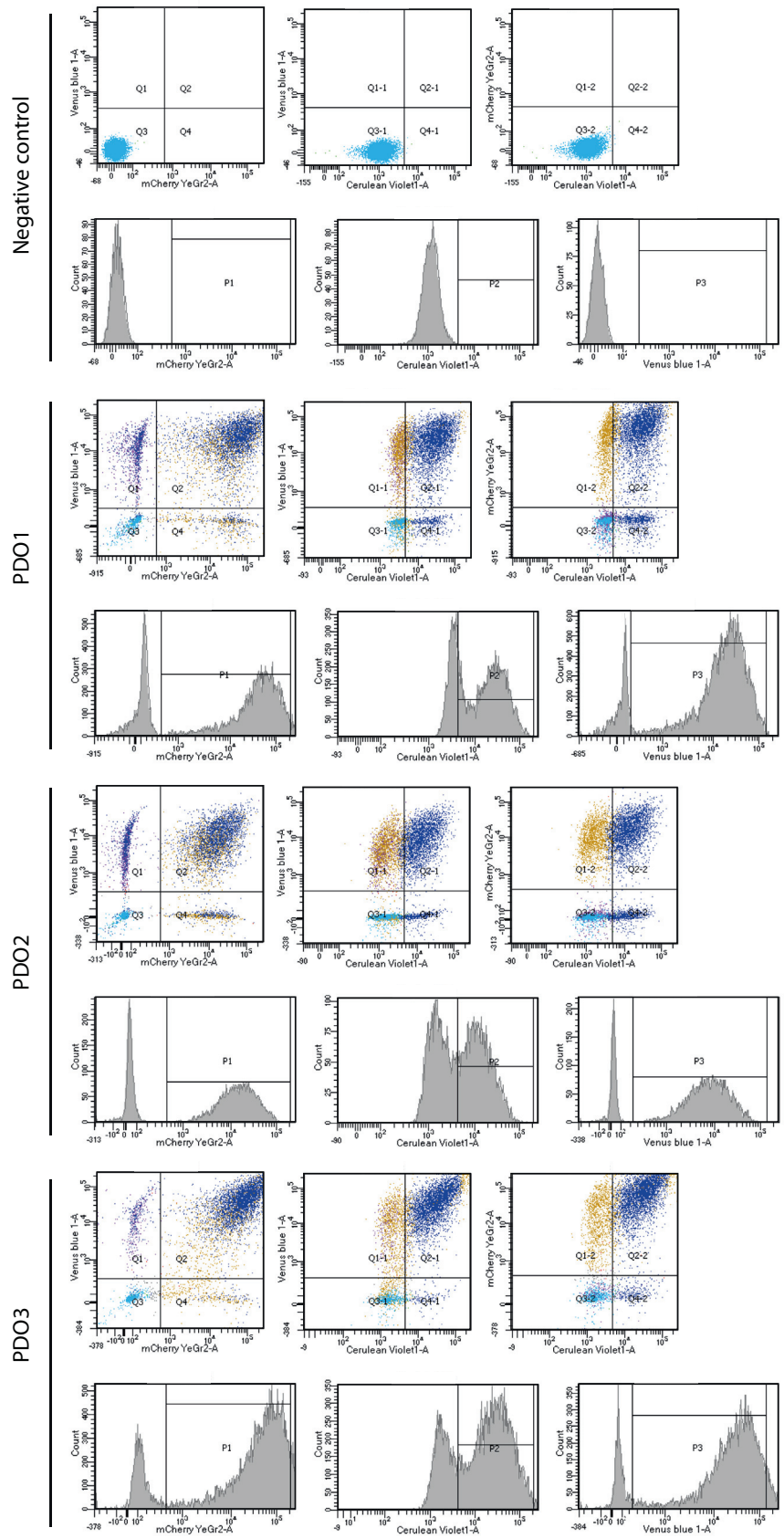
Supplementary Figure 2. Fluorescence-activated cell sorting of PDOs transduced with LeGO vectors. Gating strategy for sorting color labeled PDO1, PDO2, or PDO3 with LeGO-C2 (*red*), LeGO-V2 (*green*), LeGO-Cer2 (*blue*). Two weeks after lentiviral transduction, 1×10^6 cells of each PDO are sorted based on mCherry, Venus, and Cerulean expression using YeGr2-A, blue 1-A, and Violet1-A, respectively.
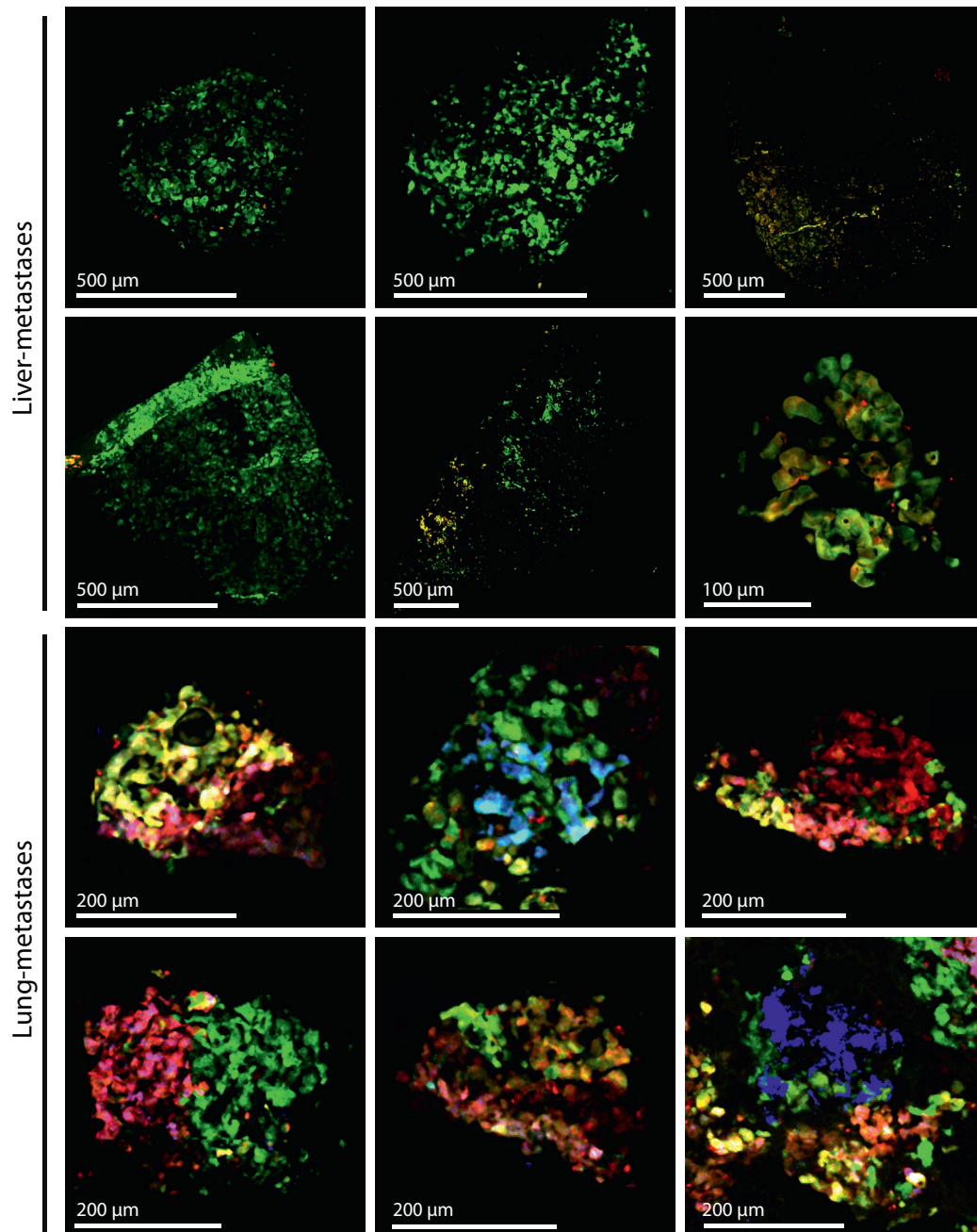
Supplementary Figure 3. Intra-lesion heterogeneity in lung metastases, but not in paired liver metastases. Representative *images* of liver (*top*) or lung metastases (*bottom*) in PDO2 model upon orthotopic caecum implantation. All *images* are derived from 1 individual mouse. *Scale bars:* 100, 200, and 500 μm.
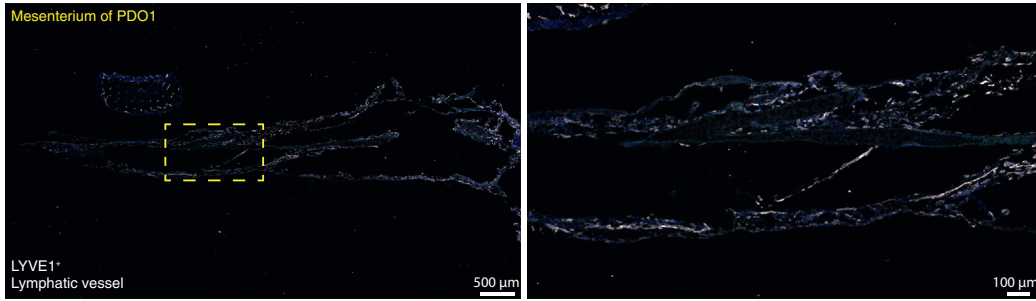
Supplementary Figure 4. Absence of tumor cell clusters in the mesenteric lymphatic vasculature of PDO1 tumor-bearing mice. En-bloc fixation on the complete mouse digestive system and immunofluorescence staining with LYVE1 demonstrates no tumor cell clusters in lymphatic vessels in mouse model PDO1.

PDO2 vs. PDO1
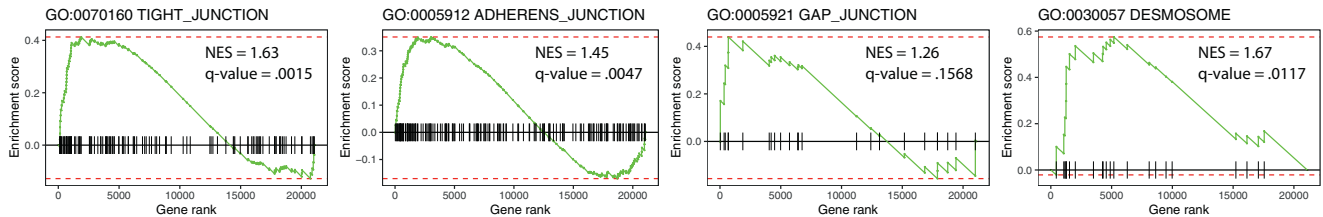
## PDO3 vs. PDO1
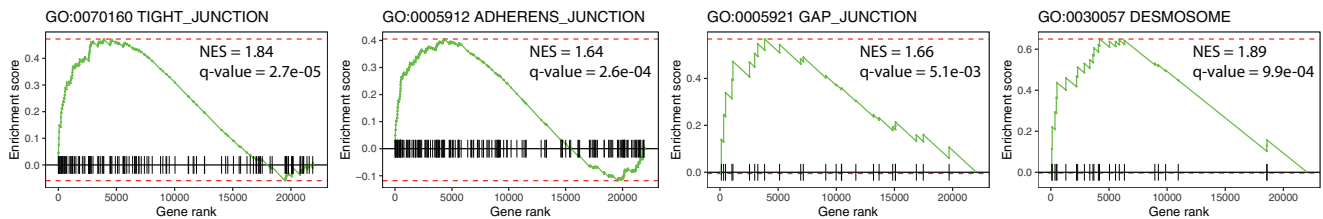
PDO2 vs. PDO3
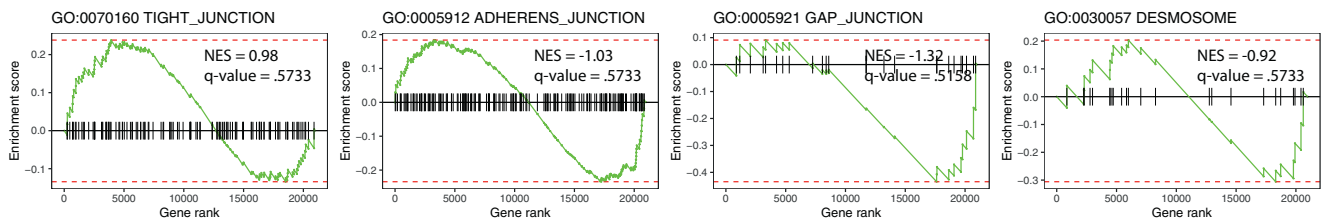
Supplementary Figure 5. Gene set enrichment analysis (GSEA) on primary cecum tumors. GSEA demonstrating significant differences in enrichment in tight, adherens, gap junction, and desmosome gene sets, between primary cecum tumors of PDO2 and 3 vs PDO1. NES, normalized enrichment score.
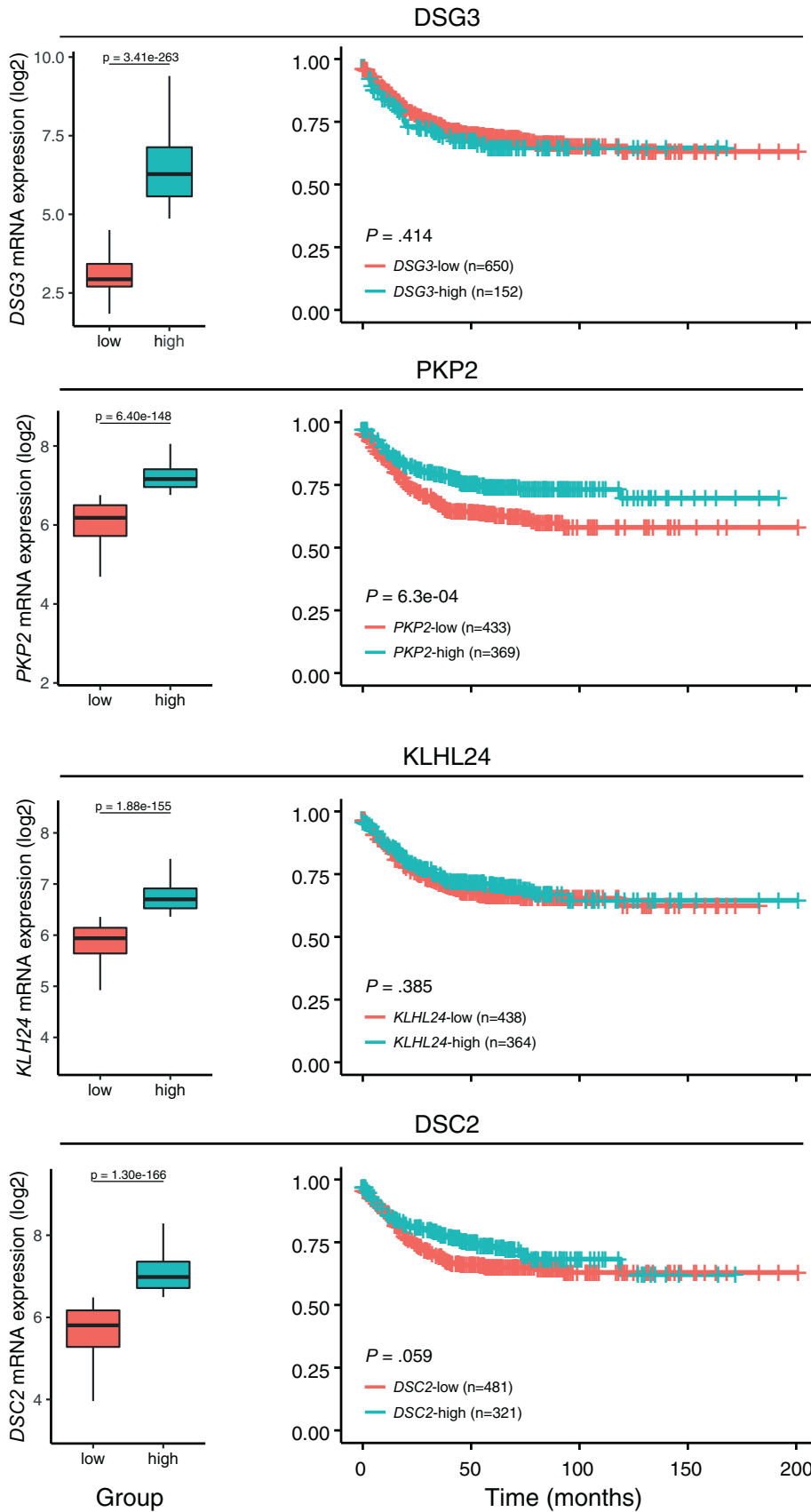
Supplementary Figure 6. Kaplan-Meijer analysis of desmosome-related genes in patients with CRC. *Box plot* represents messenger RNA expression level (log2) of *DSG3*, *PKP2*, *KLHL24*, and *DSC2* in the CMS-3232 transcriptome cohort.[28] Low- and high-expression groups are defined by the R2 function "Kaplan Meier" with cutoff mode parameter "average." Kaplan-Meier curves represent relapse-free survivals in low (*red*) and high groups (*blue*) for corresponding gene. A 2-sided log-rank test was applied to assess the significance of the survival differences between the 2 groups.
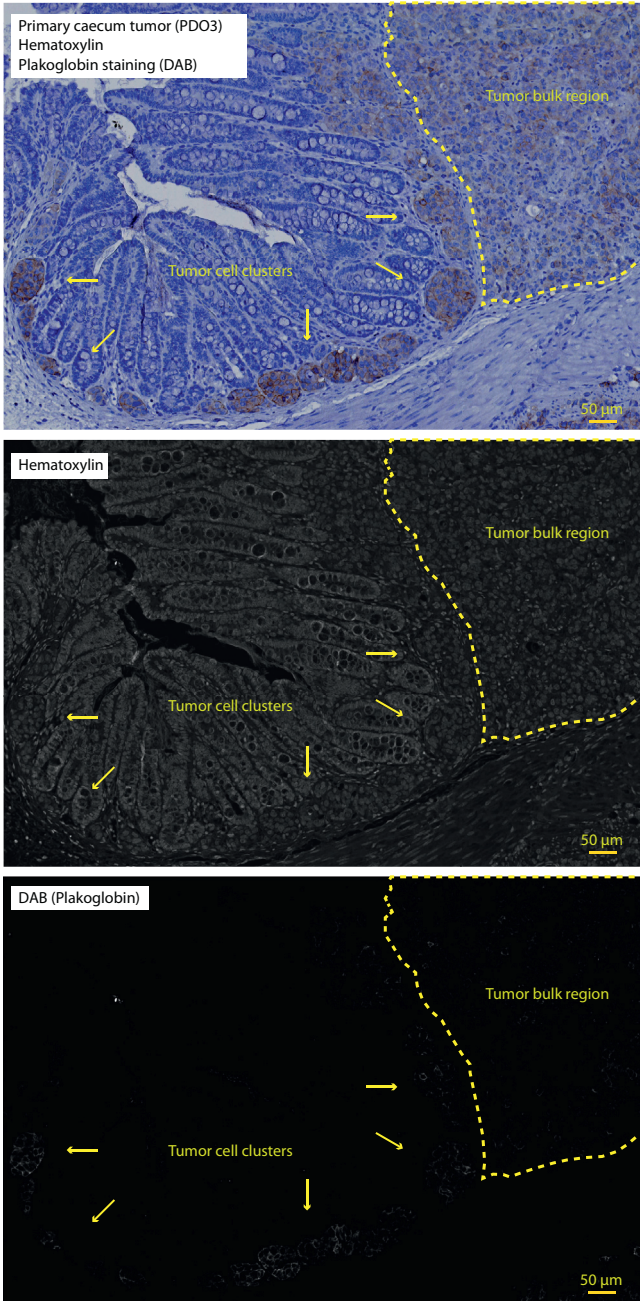
Supplementary Figure 7. Plakoglobin expression is restricted to tumor cell clusters. Histologic example of a primary cecum tumor (PDO) demonstrating that plakoglobin expression is largely restricted to tumor cell clusters. *Top* represents hematoxylin and DAB (plakoglobin) staining. *Middle* and *bottom images* represent hematoxylin (grayscale) and DAB (grayscale) staining, respectively. *Scale bar:* 50 μm. *Dashed yellow line* indicates the tumor bulk region in the cecum. *Yellow arrows* indicate tumor cell clusters apart from the bulk region.

PDO3 *in vitro* single-cell RNA seq
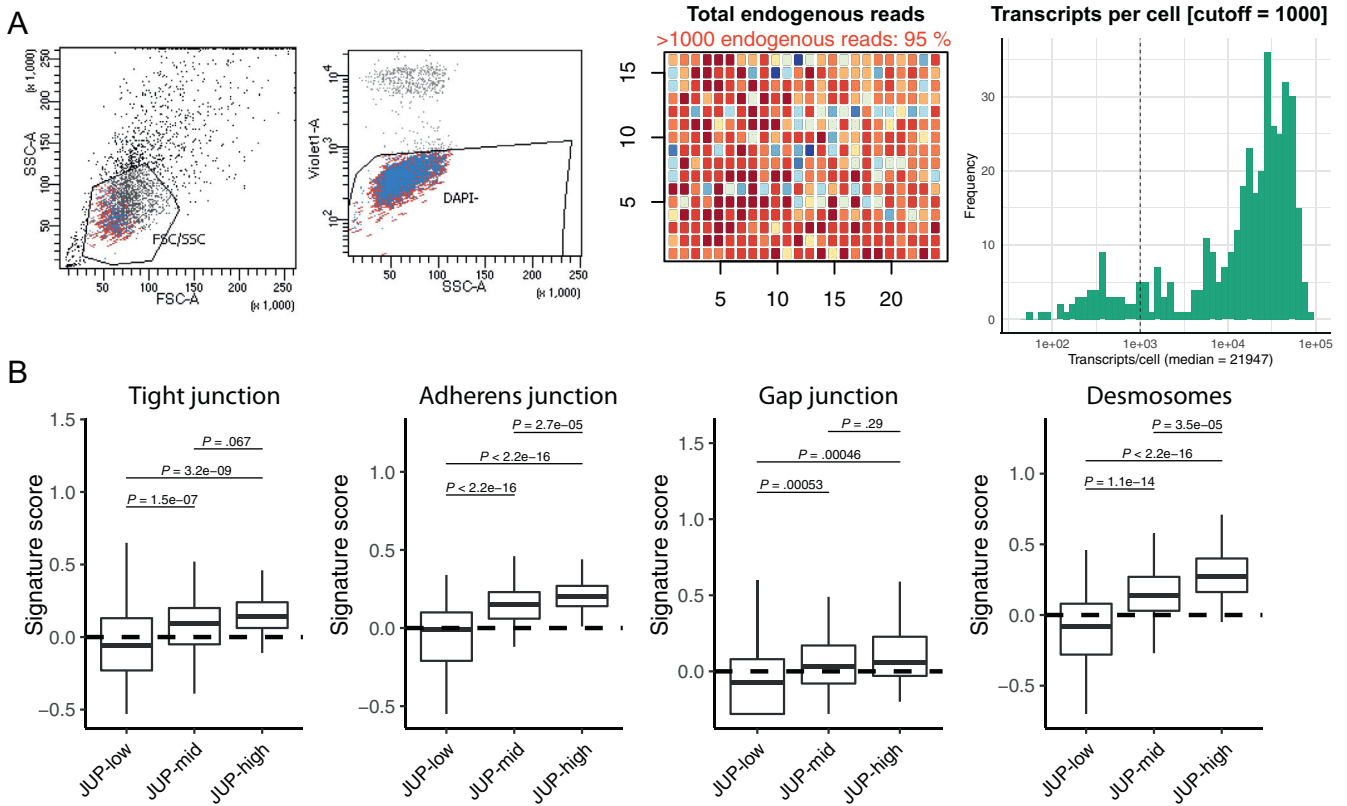
Supplementary Figure 8. Fluorescence-activated single cell sorting of in vitro cultured PDO3 cells and transcriptome analysis. (*A*) Gating strategy of sorting in vitro PDO3 cells for single-cell transcriptome profiling. The 386-well plate represent level of endogenous reads sequenced per single cell/well. *Histogram plot* represents the frequency of transcript per cell. (*B*) PDO3 single cells are classified as *JUP*-low, *JUP*-mid, and *JUP*-high based on *JUP* messenger RNA expression. Relative scores are calculated for the junction gene set signatures "Tight," "Adherens," "Gap," and "Desmosomes" (Gene Ontology IDs: 0070160, 0005912, 0005921, and 0030057). Mann Whitney U test was applied to assess the significance.
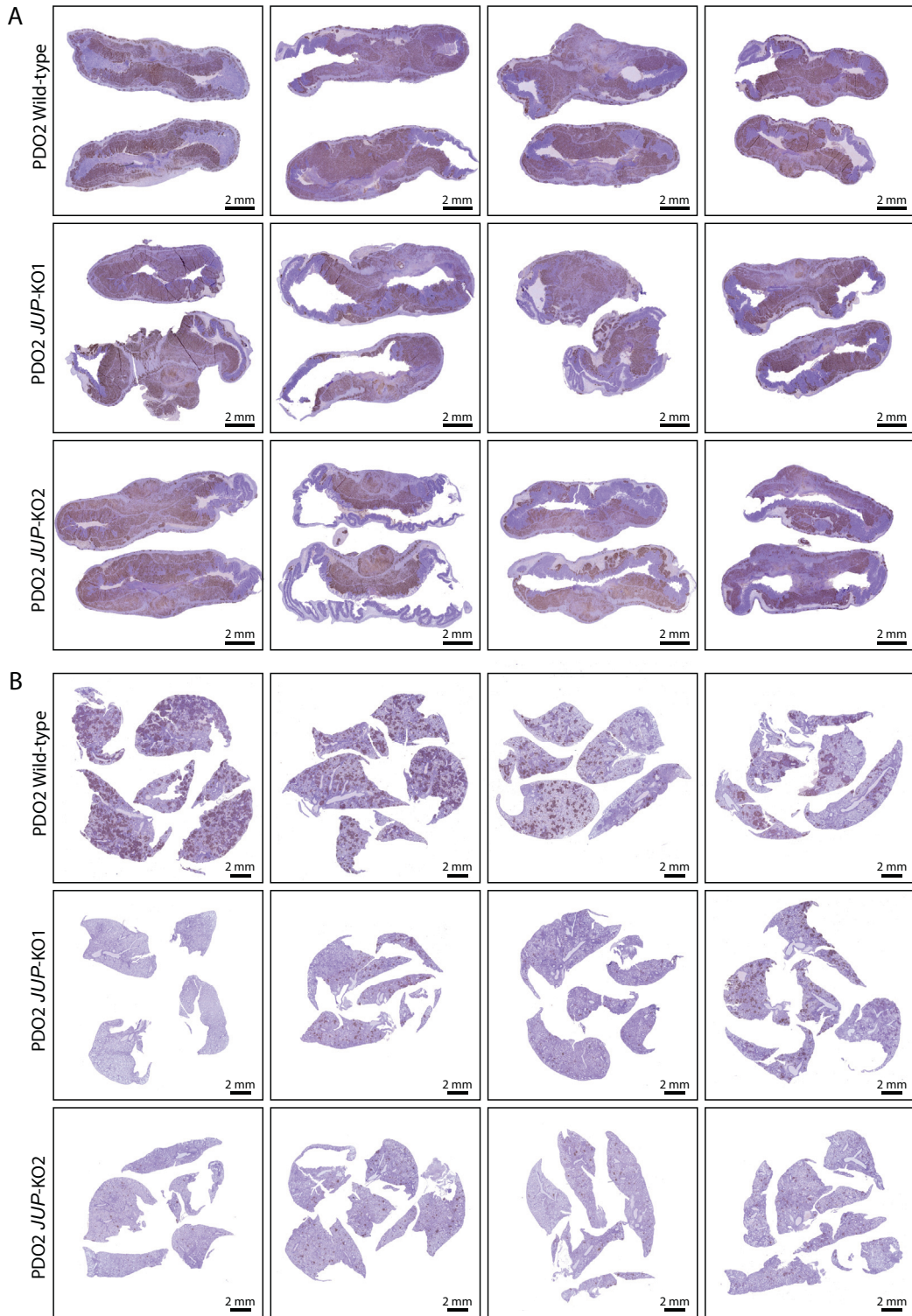
Supplementary Figure 9. Histologic overview of primary tumor and lung metastasis load in PDO2, JUP-KO1, and JUP-KO2 tumor-bearing mice. *Images* of hNucleoli immunohistochemistry staining in (*top*) primary cecum tumor and (*bottom*) lungs. *Rows* represent distinct PDO2 variants. *Scale bar:* 2 mm.

A

Control   anti-VEGFR3

Primary caecum tumor

B
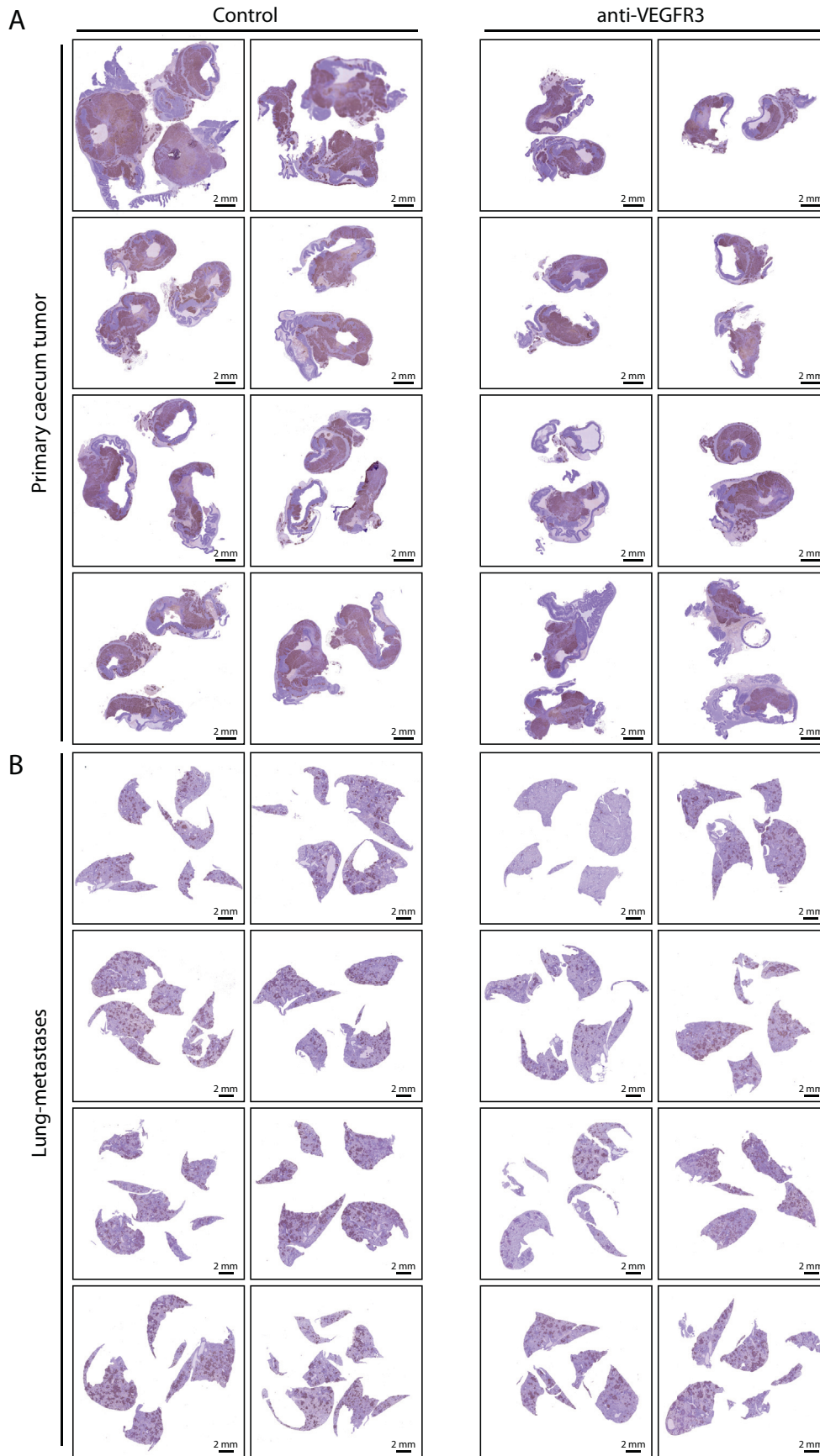
Lung-metastases

Supplementary Figure 10. Histologic overview of primary tumor and lung metastasis load in PDO2 tumor-bearing mice after saline- or anti-VEGFR3 treatment. *Images* of hNucleoli immunohistochemistry staining in (*top*) primary cecum tumor and (*bottom*) lungs. *Scale bar:* 2 mm.
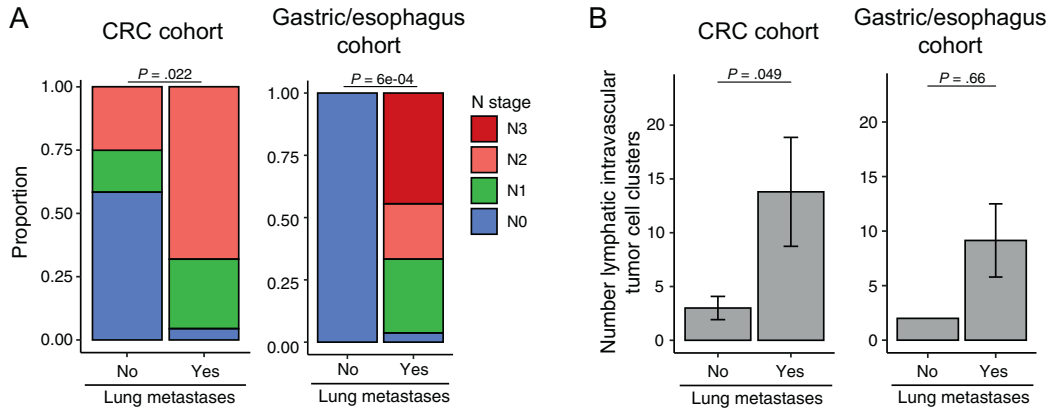
Supplementary Figure 11. Lymphatic intravascular tumor cell clusters and N-stage in tumors with or without lung metastases. (*A*) *Stacked bar plot* represent frequency of N-stage (N0, N1, N2 or N3) of CRC cohort with patients without (n = 12) or with lung metastases (n = 12). Gastric/esophagus cohort consists of patients without (n = 8) or with lung metastases (n = 10). Fisher exact test was applied. (*B*) *Bar plot* represents the mean of lymphatic intravascular tumor cell clusters. Mann-Whitney U test was applied.
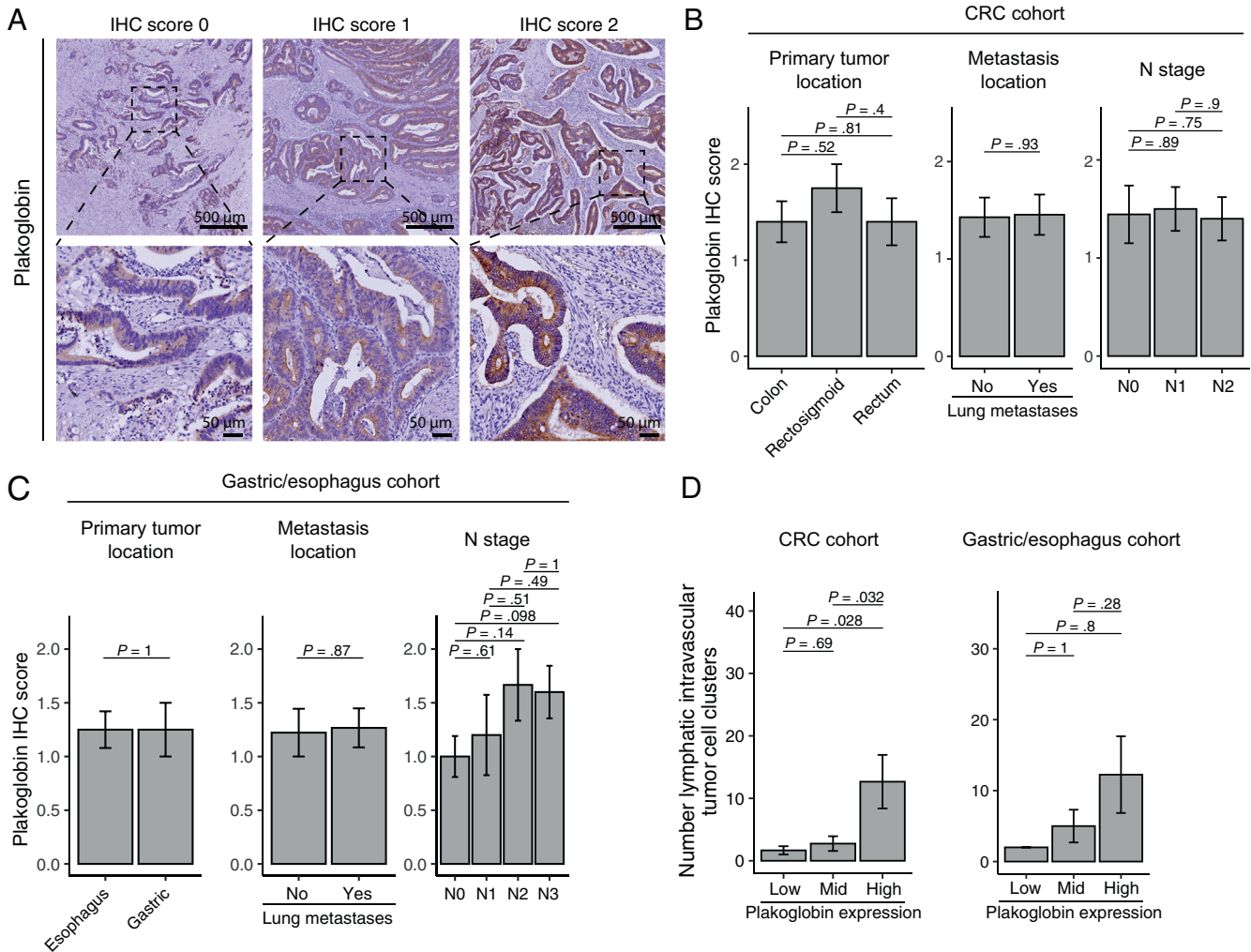
Supplementary Figure 12. Plakoglobin association with tumor location, metastasis location, N-stage, and lymphatic intravascular tumor cell clusters. (*A*) Immunohistochemistry analysis of plakoglobin expression in tumors. Examples show tumors with weak (0), intermediate (1), and strong (2) plakoglobin expression. *Scale bars:* 500 and 50 mm. (*B*) As in (*A*), *bar plots* showing the average plakoglobin staining intensity per clinical parameter: primary tumor location, lung metastases presence, or N-stage in the CRC cohort. Mann-Whitney U test was applied. (*C*) Same as (*B*), but for gastric/esophagus cohort. (*D*) *Bar plot* represents the mean of lymphatic intravascular tumor cell clusters in plakoglobin-low, -mid, and -high tumors. Mann-Whitney U test was applied.
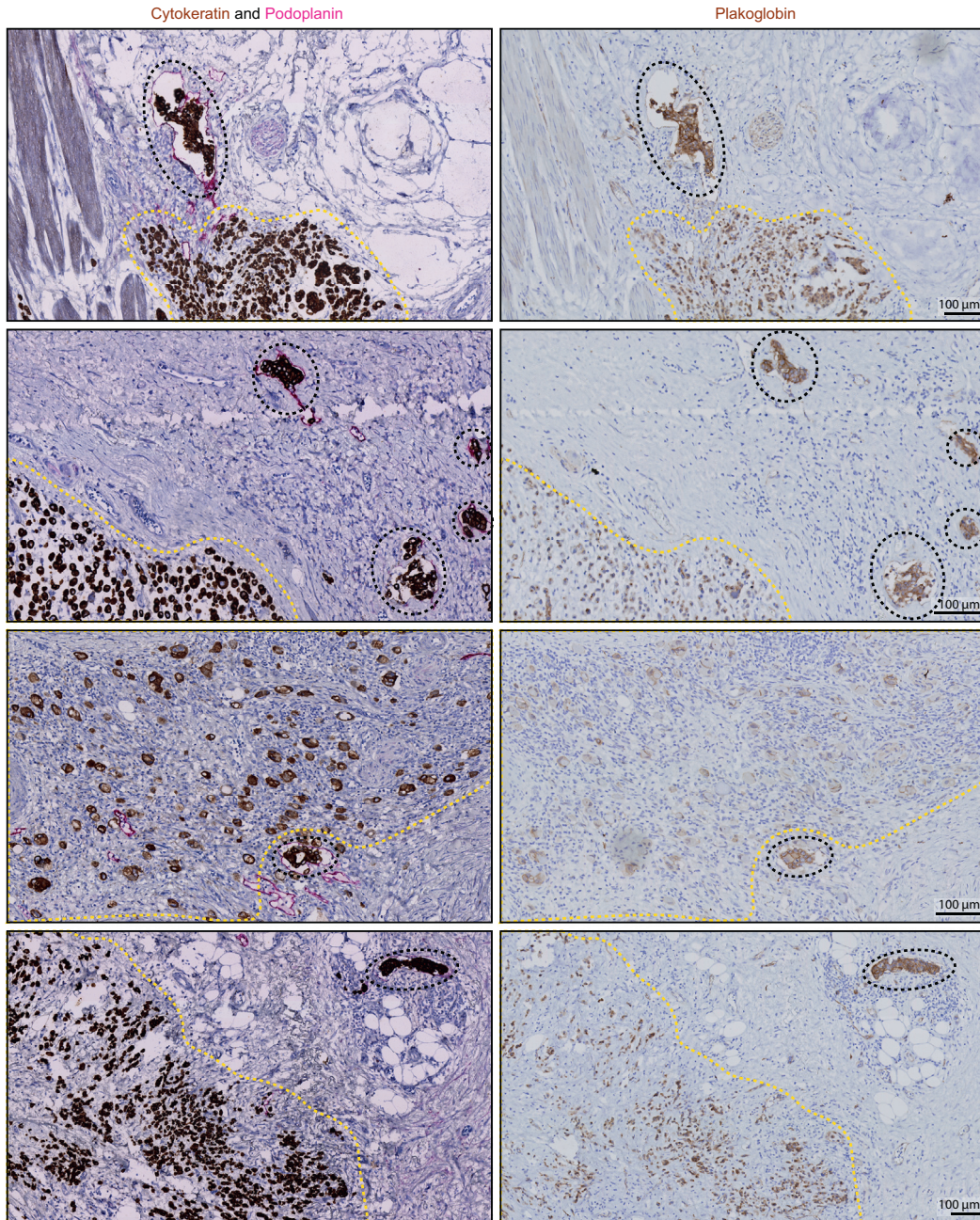
Supplementary Figure 13. Lymphatic intravascular tumor cell clusters express high plakoglobin. Examples of histologic co-staining (*left*) of pan-cytokeratin (*brown*), podoplanin (*pink*), and (*right*) plakoglobin staining (*brown*) shown. *Dashed black ellipses* represent lymphatic intravascular tumor cell clusters and other noninvading tumor cells are in indicated in *yellow dashed areas*. *Scale bar:* 100 μm.